Composites: Part B 40 (2009) 495–510

Contents lists available at ScienceDirect

Composites: Part B

journal homepage: www.elsevier.com/locate/compositesb

Predicting mesh-independent ballistic limits for heterogeneous targets by a nonlocal damage computational framework

Rashid K. Abu Al-Rub *, Sun-Myung Kim

Zachry Department of Civil Engineering, Texas A&M University, College Station, TX 77843, USA

ARTICLE INFO

Article history:
Received 27 December 2008
Received in revised form 15 March 2009
Accepted 18 March 2009
Available online 8 May 2009

Keywords:
A. Particle-reinforcement
B. Interface/interphase
A. Nano-structures
C. Damage mechanics
Size effect

ABSTRACT

During highly dynamic and ballistic loading processes, large inelastic deformation associated with high strain rates leads, for a broad class of heterogeneous materials, to degradation and failure by localized damage and fracture. However, as soon as material failure dominates a deformation process, the material increasingly displays strain softening and the finite element predictions of ballistic response are considerably affected by the mesh size. This gives rise to non-physical description of the ballistic behavior and mesh-dependent ballistic limit velocities that may mislead the design of ballistic resistant materials. This paper is concerned with the development and numerical implementation of a coupled thermo-hypoelasto-viscoplastic and thermo-viscodamage constitutive model within the laws of thermodynamics in which an intrinsic material length scale parameter is incorporated through the nonlocal gradient-dependent damage approach. This model is intended for impact and ballistic penetration and perforation problems of heterogeneous metallic targets such as metal matrix composites with dispersed particles at decreasing microstructural length scales. An evolution equation for the material length scale as a function of the material microstructural features (e.g. mean grain size in polycrystalline materials or particle size and inter-particle spacing in metal matrix composites), course of plastic deformation, strain hardening, strain-rate hardening, and temperature is presented. It is shown through simulating plugging failure in ballistic penetration of high-strength steel targets of different thicknesses by a hard blunt projectile that the length scale parameter plays the role of a localization limiter allowing one to obtain meaningful values for the ballistic limit velocity independent of the finite element mesh density. It is also shown that a local damage model incorporating viscosity and heat conduction as localization limiters, which are known to implicitly introduce length scale parameters, is insufficient in illuminating the mesh sensitivity at impact velocities close to the ballistic limit and that the mesh sensitivity increases as the target thickness increases. Therefore, the proposed nonlocal damage model leads to an improvement in the modeling and numerical simulation of high velocity impact related problems.

1. Introduction

In light of the increasing requirements for lightweight vehicular and personal protection systems in many industries (e.g. military, defense, and space), low-density advanced composite materials are highly desirable. Examples of those materials are metallic alloys, ceramics, and polymers with heterogeneous microstructures reinforced with hard, stiff, and/or soft particles (inclusions) at decreasing microstructural length scales that range in size from few nanometers (e.g. carbon nanotubes) to few microns (e.g. ceramic or metallic oxide particles). The focus of this study is on the use of those materials to increase the ballistic performance of structural systems under high impact damage loading conditions. Therefore, it is imperative to develop very effective constitutive and computational models that can be used in guiding the design processes of those advanced materials under ballistic loading conditions. The development of such models is also motivated by the large time and money cost of conducting ballistic experiments on such advanced materials such that physically based and effective theoretical and computational models, as an adjunct to experimental work, can save a lot of this cost and also provide important insights about their ballistic behaviors that are not accessible by experimental routs. Moreover, the accuracy and computational effectiveness of these models are crucial for designing better materials. Therefore, the focus of this paper is on the development of these modeling techniques that specifically address two main important issues: (1) the size-effect of microstructural features on the ballistic performance of low-density advanced materials and (2) the finite element mesh-dependent ballistic limit velocity predictions. Those two issues cannot be addressed sufficiently when using the classical (local) plasticity or viscoplasticity (rate-dependent plasticity) and damage or viscodamage (rate-dependent damage) theories due to the absence of *explicit* intrinsic material

* Corresponding author. Tel.: +1 979 862 6603; fax: +1 979 845 6554.
E-mail address: rabualrub@civil.tamu.edu (R.K. Abu Al-Rub).

1359-8368/$ - see front matter © 2009 Elsevier Ltd. All rights reserved.
doi:10.1016/j.compositesb.2009.03.009

length scale measures in their constitutive equations. Recently, the first issue (i.e. size effect) has slightly been addressed by the current authors [6,7] and heavily addressed by Clayton and coworkers (e.g. [11–13,34]). Therefore, the second issue (i.e. mesh-dependency of the ballistic limit predictions), which is to the best knowledge of the current authors has not been addressed in the literature, will be the focus of this paper.

By now, it is well-known that the use of classical (local) rate-independent plasticity and damage theories leads to numerical stability problems such as the inherent discretization dependence and finite element mesh-sensitivity in problems exhibiting plastic strain and damage localization phenomena. This is clearly an undesirable state of affairs and stems from the absence of intrinsic material length scale measures in the local constitutive equations. For the last three decades, several localization limiters (i.e. as means of preserving the well-posedness and discretization sensitivity in (initial) boundary value problems for strain softening media) that introduce explicit or implicit length scale measures have been proposed in the literature to accommodate this problem. They include but are not limited to: *rate-dependent models* (e.g. [23,24,33,45,41]) and *nonlocal gradient-dependent models* (e.g. [15,16,25,28,17,26,39,40]). Rate-dependent models implicitly possess a length scale parameter through the viscosity or fluidity parameter [33], but cannot be used to predict size-scale effects. Also, it is shown in this paper that rate-dependency is insufficient to solve the mesh-dependency problem of ballistic limit predictions. On the other hand, the nonlocal gradient-dependent approach explicitly introduces material length scale measures through the incorporation of higher-order gradient terms for microstructural internal state variables allowing one to predict size-scale effects and obtain mesh-objective results when damage localization and failure are simulated numerically. For more details about the nonlocal gradient-dependent theory and the localization limiters, see Ref. [35].

Until now the nonlocal gradient-dependent approach has been heavily used in solving strain and damage localization problems under quasi-static loading conditions. On the other hand, Voyiadjis and Abu Al-Rub (see e.g. [39,40,4]) have extended this approach to low and highly dynamic loading conditions. However, in their work, nonlocality has been introduced through plasticity and damage internal state variables with several length scale measures that are very difficult to identify from experimental data. In this paper, the theoretical framework presented in Abu Al-Rub and Voyiadjis [4] and Voyiadjis and Abu Al-Rub [43] is simplified to introduce nonlocality through one internal state variable, which is the damage density or damage variable in the continuum damage mechanics framework such that the local micro-damage nucleation, growth, and long-range microstructural interactions are incorporated. Moreover, the effect of this nonlocal damage is controlled by a material length scale parameter which is shown here to be an internal variable that is related to the dislocation's mean free path such that it evolves with the course of viscoplastic deformation, viscoplastic strain rate, temperature, and a set of microstructural parameters such as the grain size in polycrystalline materials and particle size and inter-particle spacing in particle reinforced metal matrix composites. By tailoring the values of this length scale parameter different material microstructures can be simulated as shown in Abu Al-Rub [7]. Furthermore, the damage nonlocality is cast within the context of laws of thermodynamics and finite deformation kinematics taking into account: (1) rapid time variations in temperature, inelastic strain, and strain rate, (2) shock pressure and volume changes in the equation of state, (3) thermal and damage softening, (4) heat conduction, and (5) coupling between viscoplasticity and viscodamage. Also, for the sake of completeness, the problem of numerically integrating the higher-order constitutive equations in the context of the finite element method is addressed in detail. The standard return mapping algorithm of rate-independent problems is extended to rate-dependent problems. Moreover, since the numerical implementation of the nonlocal gradient-dependent constitutive equations is not a direct task, because of the higher-order of the governing equations, a direct and simple computational algorithm for the nonlocal gradient-dependent approach is utilized.

Model capabilities in predicting meaningful values for the ballistic limit velocity independent of the mesh density are illustrated by simulating the perforation process of high-strength steel alloy targets impacted by hard blunt projectiles. Comparisons between the impact versus the residual velocity curves when treating damage as a local variable or as a nonlocal variable are presented for different target thicknesses simulated with several finite element mesh densities.

The layout of this paper is as follows: in Section 2, the nonlocal damage concept based on the gradient-dependent approach and continuum damage mechanics is presented. In Section 3, the necessary thermodynamic forces for modeling the material behavior at high strain rates, temperatures, and pressures including thermo-hypoelasto-viscoplastic and nonlocal thermo-viscodamage damage laws are derived. In Section 4, specific form for the Helmholtz free energy density and viscoplasticity and viscodamage nucleation and growth conditions are presented and the constitutive equations for the thermodynamic forces are derived. Also, in this section, failure criteria are presented. The physical interpretation for the material length scale parameter associated with nonlocal damage is discussed in Section 5. The details of the numerical implementation of the formulated constitutive equations are thoroughly discussed in Section 6. In Section 8, numerical simulations of shear plugging failure in ballistic penetration of high strength steel plate targets of different thicknesses by blunt projectiles are presented and discussed.

2. Nonlocal damage

Materials with microstructure are nonlocal in behavior due to the interplay of characteristic lengths including sizes or spacing of defect clusters, grain sizes, fiber spacing, etc. As traditional continuum mechanics does not contain explicit characteristic length scale parameters, the use of the nonlocal concept is required in order to introduce a microstructural characteristic length scale and in order to introduce long-range microstructural interactions where the stress response at a local material point is assumed to depend on the state of its neighborhood in addition to the state of the material point itself (see Fig. 1). In the current paper, the focus is on including long-range nonlocal damage interactions such that the damage state at a material point depends on its damage history

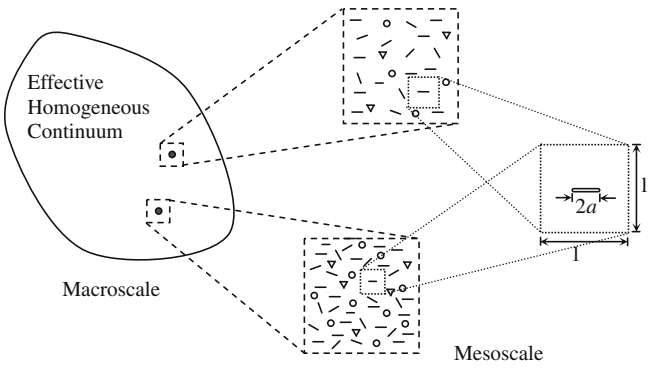

Fig. 1. Macroscopic and mesoscopic observation scales: conceptual representation of the nonlocality.

and on the damage state of the surrounding points. This can be achieved by defining the nonlocal damage density $\widehat{\phi}$ at position $\boldsymbol{x}$ as the weighted average of its local counterpart ϕ over a surrounding volume V at a small distance $|\zeta| \leqslant \ell$ from the considered point [27], such that:

$$\widehat{\phi}(\boldsymbol{x}) = \frac{1}{V_r(\boldsymbol{x})} \int_V w(\zeta)\phi(\boldsymbol{x}+\zeta)\, dV \tag{1}$$

in which

$$V_r(\boldsymbol{x}) = \int_V w(\zeta)\, dV \tag{2}$$

Superimposed hat denotes the spatial nonlocal operator, ℓ is an microstructural interaction length, and $w(\zeta)$ is a weight function that decays smoothly with distance ζ.

The integral nonlocal theory involves an infinitely extended zone of nonlocal action that may be approximated by the truncated Taylor series expansion of $\phi(\boldsymbol{x}+\zeta)$, assuming an isotropic $w(\zeta)$ (e.g. the Gauss error function of an interaction length ℓ), integrating over ℓ, and neglecting third-order and higher terms, giving rise to the gradient-dependent damage theory in which the nonlocal damage density is expressed as follows:

$$\widehat{\phi} = \phi + \ell^2 \nabla^2 \phi \tag{3}$$

where ℓ is the *internal material length scale*, which will be discussed later, and ∇^2 is the Laplacian operator. The role of the material length scale in solving the impact damage problem and in preserving the objectivity of the continuum modeling and numerical simulation of the ballistic damage problem is the main concern of this paper. The first-order gradients are disregarded since the isotropic nonlocal influence is assumed, which is represented by an isotropic weight function $w(\zeta)$. In other words, the current value of the damage density at a specific material point affects equally the damage density at the surrounding points that are located at a specific distance from that point. Moreover, the isotropy of the nonlocal weighting function is assumed here for simplicity since assuming an anisotropic weighting function (i.e. a tensor) makes the nonlocal damage density $\widehat{\phi}$ to be dependent on first- and second-order gradients. In fact, Abu Al-Rub and Voyiadjis [5] have shown that the first-order gradient is not an effective measure that can be used in obtaining mesh objective finite element results for strain localization problems due to numerical convergence problems that first-order gradients may cause.

Typically, the nonlocal gradient-dependent theory retains in the constitutive equations terms of high-order gradients of strain, plastic strain, damage density, or other internal state variables with coefficients representing length scale measures of the deformation microstructure (see Ref. [35] for more details). However, the focus of this paper is on investigating the role of Eq. (3) on the ballistic impact response of heterogeneous metallic targets perforated by blunt projectiles.

Classical (local) continuum damage mechanics based on the effective stress space [21] assumes that the effective Cauchy stress tensor, $\bar{\sigma}$, in the effective (undamaged) configuration is expressed by:

$$\bar{\sigma}_{ij} = \frac{\sigma_{ij}}{(1-\phi)^{\beta}} \tag{4}$$

where σ is the nominal Cauchy stress tensor, ϕ is interpreted as the effective surface density of micro-damage (micro-cracks and micro-voids) per unit volume (e.g. [37,36]), and $\beta > 1$ is a material parameter characterizing the effect of damage evolution on the degradation in the material's strength and stiffness. Most of the literature on continuum damage mechanics assumes $\beta = 1$ in agreement with the damage approach of Kachanov [20] for the effective (undamaged) area concept.

However, Eq. (4) is a mathematical definition of the effective stress although it may be interpreted as the uniform (average) stress acting on an effective area of the material. In order to give it a general physical meaning, it is necessary to use the corresponding damage-free material (i.e. virgin or intact material) in the mesoscale to represent the 'effective' concept of Eq. (4) for a macroscopically damaged material (see Fig. 1). Thus, a proper correlating hypothesis between two material scale levels can be obtained through using the nonlocal damage variable $\widehat{\phi}$ in Eq. (1) or (3). It is then important to emphasize that Kachanov's definition given by Eq. (4) can be generalized to a nonlocal one, for the case of isotropic damage and under a general state of stress, as follows:

$$\bar{\sigma}_{ij} = \frac{\sigma_{ij}}{\left(1-\widehat{\phi}\right)^{\beta}} \tag{5}$$

The transformation from the effective configuration to the damaged one can be done by utilizing either the strain equivalence hypothesis [22] or the strain energy equivalence hypothesis [32]. However, for the sake of simplicity and easiness in the numerical implementation, in this work the strain equivalence hypothesis is adopted, which basically states that the strains in the damaged and effective configurations are equal. Therefore, using the Hooke's law in the effective and damaged configurations, one can express the damaged elasticity fourth-order tensor, E, in terms of the corresponding effective (undamaged) elasticity tensor, $\bar{E}$, as follows:

$$E_{ijkl} = \left(1-\widehat{\phi}\right)^{\beta} \bar{E}_{ijkl} \tag{6}$$

where, for isotropic materials, $\bar{E}$ is given by:

$$\bar{E}_{ijkl} = \bar{K}\delta_{ij}\delta_{kl} + 2\bar{G}\left(\delta_{ik}\delta_{jl} - \frac{1}{3}\delta_{ij}\delta_{kl}\right) \tag{7}$$

For the virgin material, $\bar{K}$ is the bulk modulus and $\bar{G}$ is the shear modulus.

It is noteworthy that a value of $\beta > 1$ should be identified in Eqs. (5) and (6), which is not in agreement with the effective area (undamaged) concept by Kachanov [20], for the following reasons: (1) the experimental data by Voyiadjis and Venson [37] and Voyiadjis et al. [36] have shown that the damaged stiffness varies nonlinearly with the damage density, where such behavior cannot be obtained by assuming $\beta = 1$; (2) although assuming the elastic energy density equivalence hypothesis for transformation from the effective (undamaged) configuration to the nominal (damaged) configuration will yield the desired result in (1) [42], the strain equivalence hypothesis is adapted in the current study for the easiness in the numerical implementation as mentioned earlier; and (3) assuming $\beta > 1$ enhances the damage nonlocality by coupling the subsequent derived constitutive equations to $\widehat{\phi}$.

3. Thermodynamic framework incorporating nonlocal damage

In this work, the strain, strain rate, temperature, pressure, and damage material dependence are all considered. Thus the dependent constitutive variables are functions of the spatial elastic strain tensor, $\boldsymbol{e}^e$, the absolute temperature, T, the temperature gradient vector, ∇T, the measure of volumetric deformation, $J = \det(\boldsymbol{F}) > 0$, where $\boldsymbol{F}$ is the deformation gradient, and n_{int} – of phenomenological internal state variables. Here, two inelastic internal state variables are assumed to give sufficient details about the viscoplasticity strain hardening and strain-rate hardening, the viscodamage strain-softening and strain-rate softening, and the size of the localized damage zones. The viscoplasticity internal state variable is assumed to be the accumulative (equivalent or

effective) viscoplastic strain, $p = \int_0^t \sqrt{\frac{2}{3}\boldsymbol{d}^{vp} : \boldsymbol{d}^{vp}}\, dt$ with d^{vp} being the viscoplastic spatial rate of deformation and t is the time, associated with viscoplasticity isotropic hardening due to crystal defects such as forest dislocations. For the strain-softening regime of the material behavior, the non-homogenous states of deformation can appear as localized regions. Therefore, a suitable description of the evolution of such zones can be obtained with the use of the nonlocal damage density, $\widehat{\phi}$, in Eq. (3) as the viscodamage internal state variable. Hence, within the thermodynamic framework, the functional dependence of the Helmholtz free energy density, Ψ, can be expressed as:

$$\Psi = \widetilde{\Psi}\left(e^e_{ij}, T, \nabla_i T, J, p, \widehat{\phi}\right) \tag{8}$$

The internal state variables in Eq. (8) are introduced in order to provide sufficient details about the deformation defects and their local and nonlocal interactions, and to properly (i.e. physically) characterize the material microstructural behavior. The assumed dependence of Ψ on the distinct variable $\widehat{\phi}$, not its local counterpart ϕ, is also motivated by the necessity to include a length scale measure into the local continuum viscoplasticity and viscodamage equations.

Traditionally, one of the main challenges in constitutive modeling is the determination of the evolution equations for the assumed internal state variables. This can be effectively achieved through the use of laws of thermodynamics (e.g. [14,22]):

(i) Conservation of mass

$$\dot{\rho} + \rho \upsilon_{i,i} = 0 \tag{9}$$

(ii) Balance of linear momentum

$$\sigma_{ij,j} + \rho b_i = \rho \dot{\upsilon}_i \tag{10}$$

(iii) Balance of moment of momentum

$$\sigma_{ij} = \sigma_{ji} \tag{11}$$

(iv) Conservation of energy (first law of the thermodynamics)

$$\rho \dot{e} = \sigma_{ij}\dot{\varepsilon}_{ij} + \rho r_{\text{ext}} - q_{i,i} \tag{12}$$

where e can be related to Ψ through

$$e = \Psi + T\eta \tag{13}$$

(v) and the Clausius–Duhem inequality

$$\sigma_{ij} d_{ij} - \rho\left(\dot{\Psi} + \eta \dot{T}\right) - \frac{1}{T} q_i \nabla_i T \geqslant 0 \tag{14}$$

where ρ, υ, $\boldsymbol{b}$, e, r_{ext}, η, and q are the current mass density, the velocity vector, the body force vector, the internal energy density, the density of external heat, the specific entropy, and the heat flux vector, respectively.

For finite strain problems, one can assume the additive decomposition of the total rate of deformation tensor, $\boldsymbol{d}$, into thermo-elastic part, $\boldsymbol{d}^e$, and viscoinelastic part, $\boldsymbol{d}^{vi}$, such that:

$$d_{ij} = d^e_{ij} + d^{vi}_{ij} \tag{15}$$

It will be concluded later that the $\boldsymbol{d}^{vi}$ is also additively decomposed into a viscoplastic part $\boldsymbol{d}^{vp}$ due to crystal slip and a viscodamage part $\boldsymbol{d}^{vd}$ due to crack opening and void growth.

Using the multiplicative decomposition of the total deformation gradient $\boldsymbol{F}$ into a thermo-elastic part, $\boldsymbol{F}^e$, and a viscoinelastic part, $\boldsymbol{F}^{vi}$ (i.e. $\boldsymbol{F} = \boldsymbol{F}^e\boldsymbol{F}^{vi}$) and assuming incompressible viscoinelastic deformation (i.e. $J^{vi} = \det(\boldsymbol{F}^{vi}) = 1$), which is an acceptable postulate for metals, one can write the Jacobian of total deformation gradient $J = \det(\boldsymbol{F}) = J^e J^{vp} = J^e$, where $J^e = \det(\boldsymbol{F}^e)$. Hence, one can write $\dot{J}^e$ as:

$$\dot{J}^e = \frac{\partial J^e}{\partial F^e_{ij}} \dot{F}^e_{ij} = J^e d^e_{kk} \tag{16}$$

Substituting the corotational objective time derivative [designated by $\overset{\nabla}{(\,)}$] (e.g. [31]) of Eq. (8) into the Clausius–Duhem inequality in Eq. (14) along with Eqs. (15) and (16) gives:

$$\left(\sigma_{ij} - \rho \frac{\partial \Psi}{\partial e^e_{ij}}\right) d^e_{ij} + \sigma_{ij} d^{vp}_{ij} - \rho\left(\frac{\partial \Psi}{\partial T} + \eta\right)\dot{T} - \rho \frac{\partial \psi}{\partial \nabla_i T} \overset{\nabla}{\nabla_i} T - \rho \frac{\partial \Psi}{\partial J} J^e d^e_{kk} - \rho \frac{\partial \Psi}{\partial p}\dot{p} - \rho \frac{\partial \Psi}{\partial \widehat{\phi}}\dot{\widehat{\phi}} - \frac{q_i}{T}\nabla T \geqslant 0 \tag{17}$$

Note that in Eq. (17) the corotational derivative of a scalar variable is simply its material-time derivative, whereas the corotational derivative of the spatial elastic strain tensor, $\overset{\nabla}{\boldsymbol{e}}$, defines the elastic spatial rate of deformation tensor, $\boldsymbol{d}^e$. Multiplying both sides of Eq. (17) by $J = \rho^o/\rho$, where ρ^o is the initial mass density, one can then define the following thermodynamic state laws:

$$\tau_{ij} = J\sigma_{ij} = \rho_o \frac{\partial \Psi}{\partial e^e_{ij}}, \quad P = -\rho_o \frac{\partial \Psi}{\partial J}, \quad \eta = -\frac{\partial \Psi}{\partial T}, \quad \frac{q_i}{\dot{T}} = \rho_o \frac{\partial \Psi}{\partial \nabla_i T} \tag{18}$$

$$R = \rho_o \frac{\partial \Psi}{\partial p}, \quad -\widehat{Y} = \rho_o \frac{\partial \Psi}{\partial \widehat{\phi}} \tag{19}$$

where τ is the Kirchhoff stress tensor, P is the thermodynamic pressure conjugate to the change in volume due to high energy impacts, R is the isotropic hardening drag force, $\widehat{Y}$ is the nonlocal damage force, which can be physically interpreted as the energy release rate resulting from the nonlocal elastic-damage changes in the material microstructure.

Substituting the above thermodynamic laws into Eq. (17) gives the total dissipation energy Π as follows:

$$\Pi = \tau_{ij} d^{vp}_{ij} + P J^e d^e_{kk} - R\dot{p} + \widehat{Y}\dot{\widehat{\phi}} - q_i\left[\frac{\nabla_i T}{T} + \frac{\overset{\nabla}{\nabla_i} T}{\dot{T}}\right] \geqslant 0 \tag{20}$$

Utilizing the calculus of several variables with viscoplastic and viscodamage Lagrange multipliers $\dot{\lambda}^{vp}$ and $\dot{\lambda}^{vd}$, respectively, and defining the following objective function Ω which is subjected to two constraints $f = 0$ and $g = 0$ [42]:

$$\Omega = \Pi^{vi} - \dot{\lambda}^{vp} f - \dot{\lambda}^{vd} g \tag{21}$$

where Π^{vi} is the viscoinelastic dissipation, which is given by

$$\Pi^{vi} = \tau_{ij} d^{vi}_{ij} - R\dot{p} + \widehat{Y}\dot{\widehat{\phi}} \geqslant 0 \tag{22}$$

one can then use the maximum viscoinelastic dissipation principle (e.g. [30,31]), which states that for a given state variables the actual state of the thermodynamic forces is that which maximizes the inelastic dissipation function over all other possible admissible states. Therefore, one can maximize the objective function Ω by using the necessary conditions as follows:

$$\frac{\partial \Omega}{\partial \tau_{ij}} = 0, \quad \frac{\partial \Omega}{\partial R} = 0, \quad \frac{\partial \Omega}{\partial \widehat{Y}} = 0 \tag{23}$$

Substitution of Eq. (21) into Eq. (23) and using Eq. (22) yields the following thermodynamic evolution laws:

$$d^{vi}_{ij} = \dot{\lambda}^{vp}\frac{\partial f}{\partial \tau_{ij}} + \dot{\lambda}^{vd}\frac{\partial g}{\partial \tau_{ij}}, \quad \dot{p} = -\dot{\lambda}^{vp}\frac{\partial f}{\partial R}, \quad \dot{\widehat{\phi}} = \dot{\lambda}^{vd}\frac{\partial g}{\partial \widehat{Y}} \tag{24}$$

From Eq. $(24)_1$ one can assume that

$$d^{vi}_{ij} = d^{vp}_{ij} + d^{vd}_{ij} \tag{25}$$

where $\boldsymbol{d}^{vp}$ and $\boldsymbol{d}^{vd}$ define the viscoplastic and viscodamage deformation rates, such that

$$d_{ij}^{vp} = \dot{\lambda}^{vp}\frac{\partial f}{\partial \tau_{ij}}, \quad d_{ij}^{vd} = \dot{\lambda}^{vd}\frac{\partial g}{\partial \tau_{ij}} \tag{26}$$

In Eqs. (21), (24) and (26), the functions f and g are, respectively, the dynamic viscoplastic and dynamic viscodamage loading surfaces that will be defined later. Moreover, it is assumed that the microdamage processes are affected by viscoplasticity and since viscoplasticity only affects the undamaged material, the term $\partial f/\partial \widehat{Y}$ is absent from Eq. $(24)_3$.

4. Constitutive modeling

4.1. Helmholtz free energy

A generic hypoelasto-thermo-viscoplastic and thermo-nonlocal-viscodamage constitutive equations based on the general thermodynamic framework developed in the previous sections is formulated now. The energy, Ψ, in Eq. (8) can then be postulated as follows [39,40,4]:

$$\begin{aligned}\rho_o\Psi = {} & \frac{1}{2}\left(1-\widehat{\phi}\right)^{\beta} e_{ij}^{e}\overline{E}_{ijkl}e_{kl}^{e} - 3\left(1-\widehat{\phi}\right)^{\beta}\overline{K}\alpha_t e_{kk}^{e}(T-T_r) \\ & - \frac{1}{2\dot{T}}k(\nabla_i T)^2 + c_v(T^{ig}-T_r) - \frac{\rho_o}{2T_r}c_p(T-T_r)^2 \\ & - \rho_o\eta_r(T-T_r) + Q\left[p + \frac{1}{a}\exp(-ap)\right]\end{aligned} \tag{27}$$

where $\overline{\boldsymbol{E}}$ is the fourth-order elasticity tensor as defined in Eq. (7), α_t is the coefficient of thermal expansion, T_r is the reference temperature, k is the heat conductivity coefficient, c_v is the specific heat at constant volume, c_p is the specific heat at constant pressure, η_r is the reference entropy, Q (has a unit of a stress) and a (is dimensionless) are material constants characterizing the saturated isotropic hardening stress and hardening rate, respectively, and T^{ig} is chosen to have the form of the ideal gas temperature, which can be expressed as follows:

$$T^{ig} = T_r[1+\varepsilon]^{(\gamma-1)}\exp\left[\frac{\eta-\eta_r}{c_v} - \frac{(\gamma-1)\varepsilon}{1+\varepsilon}\right] \tag{28}$$

In the above equation, $\gamma = c_p/c_v$ is the ratio of the specific heats. Both c_v and c_p are related to the gas constant $\Re$ by $\Re = c_p - c_v$. The above expression is postulated in order to derive an expression for the equation of state, which relates pressure to specific density. In Eq. (28) ε is the nominal volumetric elastic strain, which can be expressed in terms of $J = J^e$ as follows:

$$\varepsilon = \frac{1}{J^e} - 1 \tag{29}$$

The constitutive equations for the thermo-elastic Kirchhoff stress tensor, Eq. $(18)_1$, can be expressed from the thermodynamic free energy, Eq. (27), as follows:

$$\tau_{ij} = \left(1-\widehat{\phi}\right)^{\beta}\left[\overline{E}_{ijkl}e_{kl}^{e} - 3\overline{K}\alpha_t(T-T_r)\delta_{ij}\right] \tag{30}$$

where, similar to Eq. (5), the Kirchhoff stress in the damaged configuration is related to its counterpart in the undamaged configuration by $\boldsymbol{\tau} = \left(1-\widehat{\phi}\right)^{\beta}\bar{\boldsymbol{\tau}}$. The spatial elastic strain is defined as $2e^e = \mathbf{1} - \boldsymbol{F}^{e^{-T}}\boldsymbol{F}^{e^{-1}}$, where $\mathbf{1}$ is the second-order unity tensor (i.e. the same as the Kronecker delta δ_{ij}) and the superimposed^{T} designates transpose and superimposed^{-1} designates inverse.

Operating on the stress relation of Eq. (30) with the corotational time derivative yields:

$$\overset{\nabla}{\tau}_{ij} = E_{ijkl}\left(d_{kl} - d_{kl}^{vp} - d_{kl}^{vd}\right) - A_{ij}\dot{\widehat{\phi}} - C_{ij}\dot{T} \tag{31}$$

where the second-order tensors $\boldsymbol{A}$ and $\boldsymbol{C}$ are given by

$$A_{ij} = \beta\left(1-\widehat{\phi}\right)^{-1}\left[E_{ijkl}e_{kl}^{e} - 3K\alpha_t(T-T_r)\delta_{ij}\right], \quad C_{ij} = 3K\alpha_t\delta_{ij} \tag{32}$$

In the effective undamaged configuration, the corotational rate of the effective Kirchhoff stress, $\bar{\tau}$, can be written from Eq. (30) and $\boldsymbol{\tau} = \left(1-\widehat{\phi}\right)^{\beta}\bar{\boldsymbol{\tau}}$ as

$$\overset{\nabla}{\bar{\tau}}_{ij} = \overline{E}_{ijkl}\left(d_{kl} - d_{kl}^{vp} - d_{kl}^{vd}\right) - 3\overline{K}\alpha_t\delta_{ij}\dot{T} \tag{33}$$

In obtaining Eqs. (31) and (32), use is made of Eqs. (6), (15) and (25) and $K = \left(1-\widehat{\phi}\right)^{\beta}\overline{K}$. Hence, Eq. (31) shows that softening occurs due to the thermal and damage evolution.

Using Eq. $(18)_2$, the thermodynamic pressure stress P can be expressed by:

$$P = (1-\gamma)c_v T^{ig}\varepsilon \tag{34}$$

which gives the equation of state necessary for high-impact loading. The equation of state accounts for compressibility effects (changes in density).

The constitutive equation for entropy, Eq. $(18)_3$, can be expressed as follows:

$$\begin{aligned}\rho_o\eta = {} & \rho_o\eta_r + 3\left(1-\widehat{\phi}\right)^{\beta}\left[\overline{K}\alpha_t + \frac{\partial(\overline{K}\alpha_t)}{\partial T}(T-T_r)\right]e_{kk}^{e} + \rho_o c_p\left[\frac{T}{T_r}-1\right] \\ & - \frac{1}{2}e_{ij}^{e}\frac{\partial\overline{E}_{ijkl}}{\partial T}e_{kl}^{e}(T-T_r) - c_v\frac{\partial T^{ig}}{\partial T} + \beta\left(1-\widehat{\phi}\right)^{\beta-1}\left[e_{ij}^{e}\overline{E}_{ijkl}e_{kl}^{e}\right. \\ & \left. -3\overline{K}\alpha_t e_{kk}^{e}(T-T_r)\right]\frac{\partial\widehat{\phi}}{\partial T} - Q[1-\exp(-ap)]\frac{\partial p}{\partial T}\end{aligned} \tag{35}$$

which is then used in the equation of state, Eq. (28), to calculate the thermodynamic pressure.

The constitutive equation for the heat flux vector $\boldsymbol{q}$ can be obtained from Eq. $(18)_4$ as follows:

$$q_i = -k\nabla_i T \tag{36}$$

which is the well-known Fourier heat conduction law. The negative sign indicates the heat flow is opposite to the direction of temperature increase.

The plasticity hardening law can be expressed from Eqs. $(19)_1$ and (27) as an exponential law

$$R = Q[1-\exp(-ap)] \tag{37}$$

or in an evolution form as follows

$$\dot{R} = a[Q-R]\dot{p} \tag{38}$$

The expression for the damage force $\widehat{Y}$ can be obtained from Eqs. $(19)_2$ and (27) at constant stress and temperature as follows:

$$\widehat{Y} = \beta\left(1-\widehat{\phi}\right)^{\beta-1}\left[\frac{1}{2}e_{ij}^{e}\overline{E}_{ijkl}e_{kl}^{e} - 3\overline{K}\alpha_t e_{kk}^{e}(T-T_r)\right] \tag{39}$$

However, it is desirable to express $\widehat{Y}$ in terms of $\bar{\tau} = \left(1-\widehat{\phi}\right)^{-\beta}\tau$ from Eq. (30) for the easiness of numerical implementation, such that:

$$\widehat{Y} = \frac{1}{2}\beta\left(1-\widehat{\phi}\right)^{\beta-1}\left[\bar{\tau}_{ij} - 3\overline{K}\alpha_t(T-T_r)\delta_{ij}\right]\overline{E}_{ijkl}^{-1}\left[\bar{\tau}_{kl} + 3\overline{K}\alpha_t(T-T_r)\delta_{kl}\right] \tag{40}$$

Note that β in Eqs. (39) and (40) should be >1 to maintain the nonlocality of Y.

The temperature evolution, $\dot{T}$, due to viscoinelastic (viscoplastic and viscodamage) energy dissipation, heat conduction, thermomechanical coupling, and external heat sources can be obtained from the thermo-mechanical heat equation, which can be derived as follows. Substituting the internal energy density, e, from Eq. (13)

into the first law of thermodynamics, Eq. (12), yields the following energy balance equation:

$$\rho\left(\dot{\Psi}+\eta\dot{T}+\dot{\eta}T\right)-\sigma_{ij}d_{ij}-\rho r_{\text{ext}}+\nabla_i q_i=0 \tag{41}$$

Multiplying both sides of Eq. (41) by $J=\rho_o/\rho$ and substituting the corotational time derivative of Eq. (8) into the resulting expression along with Eqs. (15), (16), (18), (19) and (25) yields the following relation:

$$\rho_o\dot{\eta}T=\tau_{ij}\left(d_{ij}^{vp}+d_{ij}^{vd}\right)+J^eP\dot{d}_{kk}^e-R\dot{p}+\widehat{Y}\dot{\widehat{\phi}}+\rho_o r_{\text{ext}}-J\nabla_i q_i+q_i\frac{\overset{\nabla}{\nabla_i T}}{\dot{T}} \tag{42}$$

Making use of Eq. (35) for the specific entropy $\eta=\tilde{\eta}(e^e,T,\nabla T,J,p,\widehat{\phi})$ and operating on $\tilde{\eta}$ with the corotational time derivative and substituting the result into Eq. (42) and then use Eq. (36) gives the thermo-mechanical heat balance equation as follows:

$$\begin{aligned}\rho_o c_p\dot{T}=&\tau_{ij}\left(d_{ij}^{vp}+d_{ij}^{vd}\right)+\left[\left(P-T\frac{\partial P}{\partial T}\right)J^e\delta_{ij}+T\frac{\partial\tau_{ij}}{\partial T}\right]d_{ij}^e\\&+\left[\widehat{Y}-T\frac{\partial\widehat{Y}}{\partial T}\right]\dot{\widehat{\phi}}-\left[R-T\frac{\partial R}{\partial T}\right]\dot{p}+\rho_o r_{\text{ext}}-J\nabla_i q_i\end{aligned} \tag{43}$$

The left-hand side of Eq. (43) represents the total thermal dissipation. The first term on the right-hand side represents the rate of viscoinelastic (coupled viscoplastic–viscodamage) work converted to heat, the second term represents the heat generation due to shock compression/dilatation-release and thermo-elastic coupling, the third term represent the rate of internal heat generation due to micro-cracks and micro-voids evolution and thermo-mechanical-damage coupling, the fourth term represent the rate of internal heat generation due to dislocation evolution and thermo-mechanical-viscoplastic coupling, the fifth term represents an external heat source such as radiation, and the last term is due to the heat conduction. If the duration of the deformation event is sufficiently short, the thermal conduction term becomes negligible, i.e. adiabatic conditions prevail.

4.2. Viscoplasticity and viscodamage nucleation and growth conditions

Once a material is damaged, further loading can only affect the undamaged (effective) region. Thus, the viscoplasticity function f in Eqs. (21), (24) and (26) is defined here in terms of the effective stresses. There are many dynamic viscoplasticity nucleation and growth conditions in the literature at high strain rates and temperatures for metals and metal alloys (e.g. [19,46,40,38,11]). Based on Perzyna unified viscoplasticity model [29], Voyiadjis et al. [40] have formulated a dynamic yield surface, very similar to Johnson–Cook model, which incorporates the important features of dynamic material behavior such as strain rate, strain rate history, temperature dependence, and nonlocal damage evolution, such that:

$$f\equiv\sqrt{3J_2}-\left[1-\widehat{\phi}\right]^{\beta}[\sigma_{yp}+R]\left[1+(\eta^{vp}\dot{p})^{1/m_1}\right][1-T^{*n_1}]\leqslant 0 \tag{44}$$

where $J_2=\tau':\tau'/2$ is the second invariant of the deviatoric part of the Kirchhoff stress tensor, τ', σ_{yp} is the initial yield stress in the undamaged state at reference temperature T_r, zero viscoplastic strain, and static strain rate (i.e. the smallest strain rate of the strain rate range considered at T_r), η^{vp} is the viscosity parameter, which is referred to as the relaxation time according to the notion given by Perzyna [29], m_1 is the viscoplastic rate sensitivity parameter, and $T^*=(T-T_r)/(T_m-T_r)$ defines the homologous temperature with n_1 being the temperature softening exponent.

The criterion in Eq. (44) is a generalization of the classical rate-independent von Mises yield criterion for rate-dependent materials. The latter can be simply recovered by imposing $\eta^{vp}=0$ (no viscosity effect), so that one has the case $f\leqslant 0$. In the elastic domain, both rate-independent and rate-dependent criteria coincide since $\dot{p}=0$. Therefore, the admissible stress states are constrained to remain on or within the elastic domain, so that one has similar to rate-independent plasticity $f\leqslant 0$. However, during the unloading process for rate-dependent behavior, $f<0$ and for a particular strain rate does not imply that the material is in the elastic domain, but it may also be in a viscoplastic state with a smaller strain rate. Also, the extended criterion given by Eq. (44)allows a generalization of the standard Kuhn–Tucker loading/unloading conditions:

$$f\leqslant 0,\quad \dot{\lambda}^{vp}\geqslant 0,\quad \dot{\lambda}^{vp}f=0 \tag{45}$$

with the generalized consistency condition for rate-dependent problems is given by:

$$\dot{\lambda}^{vp}\dot{f}=0 \tag{46}$$

For this reason, the dynamic yield surface can expand and shrink not only by softening/hardening effects, but also due to softening/hardening rate effects. Also, note that from using Eqs. (44) and $(26)_1$ into $\dot{p}=\sqrt{\frac{2}{3}\boldsymbol{d}^{vp}:\boldsymbol{d}^{vp}}$, one can show that $(\partial f/\partial\boldsymbol{\tau}):(\partial f/\partial\boldsymbol{\tau})=1.5$ and $\dot{\lambda}^{vp}=\dot{p}$. This relation can be also obtained from Eq. $(24)_2$ for which $\partial f/\partial R=-1$ since the evolution of R characterizes the radius of the yield surface in the absence of the strain rate and temperature effects (i.e. uncoupled yield surface).

Since isotropic damage is assumed in the current study (i.e. degradation in strength and stiffness is the same in different directions), the damage nucleation condition can be postulated to have the following simple form analogous to viscoplasticity condition [4], such that

$$g=\widehat{Y}-Y^{th}\left[1-B^{-1}\ln\left(1-\widehat{\phi}\right)\right][1+(\eta^{vd}\dot{p})^{1/m_2}][1-T^{*n_2}]\leqslant 0 \tag{47}$$

where $\widehat{Y}$ is given in Eq. (39), $Y^{th}=\beta\sigma_{yp}^2/2\overline{E}$, with $\overline{E}$ is undamaged Young's modulus, is the initial damage threshold at reference temperature T_r, zero damage, and static strain rate, B is a material constant characterizing the damage growth rate, η^{vd} is the relaxation time that corresponds to the damage growth, m_2 is the viscodamage rate sensitivity parameter, and n_2 is the temperature softening exponent associated with damage evolution. For generality, it is assumed here that the time- and temperature-dependent behavior of both viscoplasticity and viscodamage mechanisms are controlled by different relaxation times and strain rate and temperature softening exponents, which may not generally be the case for metallic matrices.

The admissible damage forces are constrained to remain on or within the undamaged domain, $g\leqslant 0$. Similar to the viscoplasticity surface, the rate-independent damage surface can be simply recovered by imposing $\eta^{vd}=0$ (no damage-viscous effect), so that one has $g\leqslant 0$. The model response in the viscodamage domain is then characterized by the Kuhn–Tucker complementary conditions, similar to that in Eqs. (45) and (46), as follows:

$$g\leqslant 0,\quad \dot{\lambda}^{vd}\geqslant 0,\quad \dot{\lambda}^{vd}g=0 \tag{48}$$

and the damage generalized consistency condition for rate-dependent problems is given by:

$$\dot{\lambda}^{vd}\dot{g}=0 \tag{49}$$

From Eqs. $(24)_2$ and (47), one concludes that $\dot{\lambda}^{vd}=\dot{\widehat{\phi}}$.

4.3. Failure criteria

Here, the failure criteria proposed by Abu Al-Rub and Voyiadjis [4] for high speed impact damage problems are utilized. The failure

criteria are based on both the nonlocal evolution of the accumulated micro-damage internal state variable, $\widehat{\phi}$, and the equation of state for the thermodynamic pressure, P, such that if:

$$\widehat{\phi} = \phi_c \quad \text{and/or} \quad P = P_{\text{cutoff}} \tag{50}$$

the material loses its carrying capacity, where ϕ_c is the critical damage when catastrophic failure in the material takes place and P_{cutoff} is the pressure cutoff value when tensile failure or compressive failure occurs. If either of the conditions in Eq. (50) is satisfied the stress field is assumed zero at the corresponding point. This describes the main feature observed experimentally that the load tends to zero at the fracture point. Hence, once all the integration points in an element in the finite element method fail, the whole element is eroded or deleted with the mass is conserved.

5. Physical interpretation of the material length scale

In spite of the crucial importance of the material length scale ℓ in the gradient theory (see Eq. (3)), very limited work is focused on the physical origin of this length scale parameter. The microstructural origin of ℓ is rarely clear and its value is usually a free parameter. In fact, the full utility of the gradient-dependent theory hinges on one's ability to identify values for ℓ. More importantly is the difficulty of carrying out truly definitive experiments on critical aspects of the evolution of the dislocation, crack, and void structures that reveal the physical nature of ℓ. Abu Al-Rub and Voyiadjis [2] have concluded that the determination of ℓ should be based on information from micromechanical, gradient-dominant tests such as micro- and nano-indentation tests. Moreover, Abu Al-Rub and Voyiadjis [3] presented a dislocation-based approach for the analytical identification of ℓ for metallic materials and showed that ℓ is proportional to the mean free-path for dislocation motion and is not constant but varies with the material microstructural features (e.g. mean grain size in polycrystals or the mean particle size in particle reinforced composites) and the course of plastic deformation. Moreover, they have showed for dynamic problems that ℓ decreases with increasing plastic strain, increasing strain hardening rates, increasing strain rate, and decreasing temperature, and its value is on the order of micrometers which is close to the thickness of adiabatic shear bands. The following evolution function for ℓ has been proposed:

$$\dot{\ell} = \ell v_o \exp\left[-(U_o/k_B T)\left\{1 - \left(\bar{\tau}^*/\bar{\tau}_o^*\right)^p\right\}^q\right] \tag{51}$$

where v_o is the fundamental vibration frequency of the dislocation, p and q are material constants defining the shape of the short-range obstacle, k_B is the Boltzmann's constant, U_o is the referential activation energy at zero absolute temperature, $\bar{\tau}^*$ is the undamaged thermal stress from Eq. (44), which is a function of strain p, strain rate $\dot{p}$, and temperature T,

$$\bar{\tau}^* = (\sigma_{yp} + R)(\eta^{vp}\dot{p})^{1/m_1}(1 - T^{*n_1}) \tag{52}$$

and $\bar{\tau}_o^*$ is the referential thermal stress for the intact material at which dislocations can overcome the obstacles without the assistance of thermal activation. Furthermore, ℓ has the following expression [44]:

$$\ell = \frac{dD}{D + d[1 - \exp(-ap)]} \tag{53}$$

where d is the mean grain size or mean particle (inclusion) size, D is the mean inter-particle spacing in particle reinforced composites or other characteristic size, p is the effective plastic strain, and a is the strain-hardening rate (see Eq. (37)). This equation shows that ℓ decreases with the effective plastic strain, increases with the grain size or inclusion size, decreases with the ratio of D/d, and decreases with the strain-hardening rate. It also shows that ℓ decreases from an initial value $\ell = d$ at yielding to a final value $\ell \to 0$ which corresponds to the classical local plasticity or damage limit at very large values of D, d, or p.

6. Numerical implementation

In this section, the numerical integration algorithm for implementing the proposed constitutive equations in a finite element code is developed. Let $t_o, t_1, \ldots, t_{n+1} = t_n + \Delta t$ be convenient time instances along the time interval over which the dynamic response of the body is sought. Consider the time step $\Delta t = t_{n+1} - t_n$ where at $t = t_n$ all quantities are known that are the converged values of the previous time increment, and the solution must be computed at t_{n+1} for a given body load increment, $\Delta \boldsymbol{b}$, and surface load increment, $\Delta \boldsymbol{t}$.

Let the dynamic evolution of a hypoelastic-thermo-viscoplastic and thermo-viscodamaged body of volume V and surface S be governed at step time $n+1$ (i.e. t_{n+1}), by the constitutive relations presented in the previous sections and by the following momentum, initial, and compatibility relations:

$$\boldsymbol{L}^T \boldsymbol{\tau}_{n+1} + \rho_o \boldsymbol{b}_{n+1} = \rho_o \dot{\upsilon}_{n+1} \ \text{ in } V; \boldsymbol{t}_{n+1} = \boldsymbol{\tau}_{n+1}\boldsymbol{n} \text{ on } S_t \tag{54}$$

$$\boldsymbol{u} = \boldsymbol{u}_o, \quad \upsilon = \upsilon_o \quad \text{at } t = t_o \tag{55}$$

$$\boldsymbol{l}_{n+1} = \boldsymbol{\nabla}\upsilon_{n+1} = \boldsymbol{C}\upsilon_{n+1} \ \text{ in } V \tag{56}$$

$$\boldsymbol{u}_{n+1} = \tilde{\boldsymbol{u}} \text{ on } S_u; \upsilon_{n+1} = \tilde{\upsilon} \text{ on } S_\upsilon; T_{n+1} = \widetilde{T} \text{ on } S_T; \boldsymbol{q}_{n+1} = \tilde{\boldsymbol{q}} \text{ on } S_q \tag{57}$$

where $(\bullet)_{n+1} = (\bullet)_n + \Delta(\bullet)$ is the additive decomposition of each of the internal variables. For algorithmic convenience, we have shifted to matrix vector notation in this section. Eq. (54) express the discrete dynamic motion in the volume V and equilibrium on the free part of the boundary S_t at $n+1$. Visco-hypoelasticity is not considered in this study; viscous damping effects are neglected. $\boldsymbol{L}$ is the differential operator, $\boldsymbol{b}$ and $\boldsymbol{t}$ are the body force and the surface traction vectors, respectively, $\boldsymbol{u}$ is the three-component displacement vector, and $\boldsymbol{n}$ denotes the outward normal to the surface S. The initial conditions on displacements and velocities are given by Eq. (55). Compatibility relation in volume V is given by Eq. (56). The boundaries S_u, S_υ, S_T, and S_q are parts of the boundary where the displacement $\tilde{\boldsymbol{u}}$, the velocity $\tilde{\upsilon}$, the temperature $\widetilde{T}$, and the heat flux $\tilde{\boldsymbol{q}}$ is prescribed, respectively. It is clear that $S_t \cup S_u \cup S_\upsilon \cup S_T \cup S_q = S$, $S_t \cap S_u = 0$, and $S_T \cap S_q = 0$.

In the context of the finite element method, the discrete problem can be obtained via a spatial displacement-based projection of the semi-discrete (i.e. discrete in space and continuous in time) problem into a finite dimensional subspace of admissible continuous shape functions. Consequently, in the following sections the procedure for solving the derived set of governing equations using the finite element method is described thoroughly. In order to integrate the set of constitutive equations, a return mapping algorithm is developed in the subsequent sections.

6.1. Return mapping algorithm

Considering a given configuration of known set of positions $\boldsymbol{X}$ at time t_n, the problem is now to update all state variables to a new configuration defined by its respective set of positions $\boldsymbol{x}$ (which are supposed to be known) at time t_{n+1}. This situation typically arises in a nonlinear finite element problem where the new positions $\boldsymbol{x}$ are determined from the discretized version of the momentum equation, Eq. $(54)_1$.

In this section a semi-implicit stress integration algorithm for rate-dependent problems [41] is recalled. This stress update algo-

rithm treats the rate-independent and rate-dependent problems in a unified way. It is unified in a sense that the same routines are able to integrate both rate-independent and rate-dependent models by simply setting the viscosity parameters, η^{vp} in Eq. (44) and η^{vd} in Eq. (47), to zero. Moreover, in this paper this algorithm is extended to thermo-hypo-viscoplastic and nonlocal thermo-visco-damage constitutive equations with a two-step predictor-corrector structure: thermo-hypo-elastic predictor step and a coupled viscoplastic–viscodamage corrector step. In the first step, the hypo-elastic predictor problem is solved with initial conditions that are the converged values of the previous iteration i while keeping the irreversible variables frozen. This produces a trial stress state, ${}^{tr}\boldsymbol{\tau}$, which, if outside the viscoplastic surface f and/or the viscodamage surface g is taken as the initial conditions for the solution of the viscoplastic–viscodamage corrector problem. The scope of this second step is to restore the generalized consistency condition by returning back the trial stress to the viscoplastic surface f and the viscodamage surface g simultaneously as conceptually represented in Fig. 2. Therefore, the two inelastic loading conditions, f and g, need to be satisfied simultaneously through the viscoplastic consistency condition in Eq. (46) and the viscodamage consistency condition in Eq. (49). Moreover, f and g are satisfied at the end of the loading step (i.e. in a nonlocal manner). Similar treatment for more complex constitutive equations has been presented in Voyiadjis and Abu Al-Rub [43]. The different steps of the current proposed integration algorithm are detailed below.

6.1.1. Hypo-elastic predictor

If the variables at iteration i, such as $\boldsymbol{\tau}_i$, R_i, $\widehat{\phi}_i$, $\widehat{Y}_i$, and T_i, are assumed to be determined and the values of $\boldsymbol{d}$ and Δt are given, then $\boldsymbol{\tau}_{i+1}$ that satisfies the discretized constitutive equations can be obtained. However, one of the major challenges while integrating the constitutive equations in finite deformation context is to achieve the incremental objectivity, i.e. to maintain correct rotational transformation properties all along a finite time step. A procedure that has now become very popular is first to rewrite the constitutive equations in a corotational moving frame (for more details, see Ref. [31]). Therefore, assuming that the variables of the model at iteration i and the displacement field $\boldsymbol{u} = \boldsymbol{x}_{i+1} - \boldsymbol{x}_i$ at iteration $i+1$ are known, the trial elastic stress can then be given in the corotational frame by

$$ {}^{tr}\boldsymbol{\tau}_{i+1} = \boldsymbol{R}(\boldsymbol{\tau}_i + \boldsymbol{E}_i : \boldsymbol{D})\boldsymbol{R}^T \tag{58}$$

where $\boldsymbol{R}$ is the rotation matrix, which is obtained from the polar decomposition $\boldsymbol{F} = \boldsymbol{R}\cdot\boldsymbol{U}$, and $\boldsymbol{D}$ is the (incremental) logarithmic strain tensor between the reference configuration and the current one, which is given by

$$ \boldsymbol{D} = \ln \boldsymbol{U} = \frac{1}{2}\ln \boldsymbol{U}^2 = \frac{1}{2}\ln(\boldsymbol{F}^T\boldsymbol{F}) \tag{59}$$

where $\boldsymbol{F}$ is the total deformation gradient and $\boldsymbol{U}$ is the right stretch tensor.

In the above procedure, it is essential to realize that $\boldsymbol{F} = \boldsymbol{R}\cdot\boldsymbol{U}$ are incremental tensors; in the case of rigid body motion, $\ln \boldsymbol{U} = 0$, thus the stress tensor will be updated exactly by the relation $\boldsymbol{\tau}_{n+1} = \boldsymbol{R}\boldsymbol{\tau}_n\boldsymbol{R}^T$ whatever the amplitude of the rotation. $\boldsymbol{R}$ is directly and exactly computed from the polar decomposition and only needs to be evaluated once per time step. All kinematic quantities are based on the deformation gradient $\boldsymbol{F}$ over the considered time step, a quantity that is readily available in nonlinear finite element codes such as Abaqus [1].

6.1.2. Viscoplastic and viscodamage correctors

Now if ${}^{tr}f({}^{tr}\boldsymbol{\tau}_{i+1}, R_i, \dot{p}_i, T_i, \widehat{\phi}_i) \leqslant 0$ and ${}^{tr}g({}^{tr}\widehat{Y}_{i+1}, \widehat{\phi}, \dot{p}_i, T_i) \leqslant 0$, the process is clearly undamaged elastic and the trial stress is in fact the final stress state. On the other hand, if ${}^{tr}f > 0$ and/or ${}^{tr}g > 0$, the Kuhn–Tucker loading/unloading conditions, Eqs. (45) and (48), are violated by the trial stress which now lies outside f and g (see Fig. 2). Consistency, is restored by a generalization of the classical return mapping algorithm to rate-dependent problems [41]. Since the objective rates reduce to a simple time derivative due to the fact that the global configuration is held fixed, the coupled viscoplastic–viscodamage corrector problem may then be rephrased from Eq. (31) as:

$$ \dot{\tau} = -\boldsymbol{E} : (\boldsymbol{d}^{vp} + \boldsymbol{d}^{vd}) - \boldsymbol{A}\dot{\widehat{\phi}} - \boldsymbol{C}\dot{T} \tag{60}$$

The hypoelastic predictor and coupled viscoplastic–viscodamage corrector step yields the final stress as:

$$ \boldsymbol{\tau}_{i+1} = {}^{tr}\boldsymbol{\tau}_i - \boldsymbol{E}_i : (\boldsymbol{d}^{vp} + \boldsymbol{d}^{vd}) - \boldsymbol{A}_i\dot{\widehat{\phi}} - \boldsymbol{C}_i\dot{T} \tag{61}$$

By making use of the evolution equations for $\boldsymbol{d}^{vp}$ and $\boldsymbol{d}^{vd}$ from Eqs. $(26)_1$ and $(26)_2$, respectively, into the heat equation, Eq. (43), along with $\dot{\lambda}^{vp} = \dot{p}$, $\dot{\lambda}^{vp} = \dot{\phi}$, $r_{\text{ext}} = 0$, and Eq. (3), the temperature evolution can then be reduced to:

$$ \dot{T} = \boldsymbol{Q}_1 : \boldsymbol{d} + Q_1^t\nabla^2 T + Q_1^p\dot{p} + Q_1^d\dot{\phi} + Q_2^d\nabla^2\dot{\phi} \tag{62}$$

where $\boldsymbol{Q}_1$, $Q_1^t = Jk/c_p$, Q_1^p, Q_1^d, and $Q_2^d = \ell^2 Q_1^d$ are obtained from the previous iteration i and their full expressions are given in Appendix A through Eqs. (A.1)–(A.3).

Moreover, one requires the satisfaction of the generalized viscoplasticity consistency condition $\dot{f}$, Eq. (46), at the end of iteration $i+1$. Since f is expressed in terms of the effective stresses in the undamaged configuration, one can write the viscoplastic consistency condition as follows:

$$ \dot{f} = \frac{\partial f}{\partial \bar{\boldsymbol{\tau}}}\overset{\nabla}{\bar{\boldsymbol{\tau}}} + \frac{\partial f}{\partial R}\dot{R} + \frac{\partial f}{\partial p}\dot{p} + \frac{\partial f}{\partial \dot{p}}\ddot{p} + \frac{\partial f}{\partial T}\dot{T} = 0 \tag{63}$$

Since the local iteration process is applied within the time step $t+\Delta t$ (i.e. at step $n+1$) and the updated Lagrangian formulation is used then $\dot{p} = \Delta t\ddot{p}$ can be assumed. Substitution of Eqs. (33), (38) and (62) along with Eqs. (3), (26) and (44) into Eq. (63) yields the following expression:

$$ \mathbf{Q}_2 : \boldsymbol{d} + Q_2^t\nabla^2 T + Q_2^p\dot{p} + Q_3^d\dot{\phi} + Q_4^d\nabla^2\dot{\phi} = 0 \tag{64}$$

where $\boldsymbol{Q}_2$, $Q_1^t = (Jk/c_p)\partial_T f$, Q_2^p, Q_3^d, and $Q_4^d = \ell^2 Q_3^d$ are obtained from the previous iteration i and their full expressions are given in Appendix A through Eqs. (A.4)–(A.6).

Similarly, the generalized viscodamage consistency condition $\dot{g}$, Eq. (49), needs to be satisfied. Since the viscodamage driving force

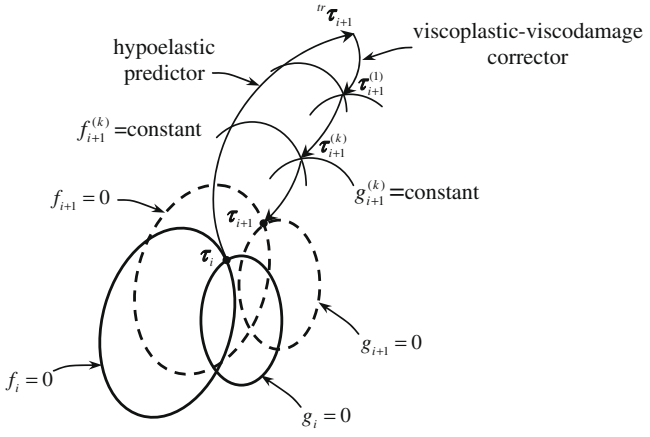

Fig. 2. Conceptual representation of the hypoelastic predictor and coupled viscoplastic–viscodamage corrector algorithm.

$\widehat{Y}$ is a function of $\bar{\tau}, \widehat{\phi}$, and T as shown in Eq. (40) and g, besides those, is a function of $\dot{p}$ as shown in Eq. (47), one can then express $\dot{g}$ as follows:

$$\dot{g} = \frac{\partial f}{\partial \bar{\tau}} \overset{\nabla}{\bar{\tau}} + \frac{\partial g}{\partial \widehat{\phi}} \dot{\widehat{\phi}} + \frac{\partial f}{\partial p} \ddot{p} + \frac{\partial f}{\partial T} \dot{T} = 0 \tag{65}$$

Substitution of Eqs. (33), (3) and (62) along with Eqs. (26) and (47) and the relation $\dot{p} = \Delta t \ddot{p}$ into Eq. (65) yields the following expression:

$$\boldsymbol{Q}_3 : \boldsymbol{d} + Q_3^t \nabla^2 T + Q_3^p \dot{p} + Q_5^d \dot{\phi} + Q_6^d \nabla^2 \dot{\phi} = 0 \tag{66}$$

where $\boldsymbol{Q}_3$, $Q_2^t = (Jk/c_p)(\partial_T f - 3\overline{K}\alpha_t \partial_\tau g : \mathbf{1})$, Q_3^p, Q_5^d, and $Q_6^d = \ell^2 Q_3^d$ are obtained from the previous iteration i and their full expressions are given in Appendix A through Eqs. (A.7)–(A.9).

Both Eqs. (62), (64) and (66) can be used to calculate $\dot{T}$, $\dot{p}$, and $\dot{\phi}$ at each local point. However, one of the most challenges of implementing a nonlocal gradient-dependent model is the numerical calculation of higher-order gradients within a local finite element code. In the following, a simple and robust numerical procedure for calculating $\nabla^2 T$ and $\nabla^2 \dot{\phi}$ in Eqs. (62), (64) and (66) is detailed based on the work of Abu Al-Rub and Voyiadjis [5].

6.2. Computation of the Laplacian

In the approach advocated by Abu Al-Rub and Voyiadjis [5], which is extended to finite strain inelasticity by Voyiadjis and Abu Al-Rub [43], the nonlocal damage consistency condition is transformed into a linear set of equations that depends on the material parameters and on the current coordinates of the integration points. These sets of linear equations are solved by any numerical iterative method for the rate of damage variable, $\dot{\phi}$, and temperature, T, at the integration points that exist in a global (nonlocal) superelement of eight adjacent local elements in a nonlocal sense (Figs. 3 and 4). The Laplacians, $\nabla^2 \dot{\phi}$ and $\nabla^2 T$, at each integration point in the local element are evaluated from the derivatives of a polynomial that interpolates the value of $\dot{\phi}$ and T in the superelement with classical integration points. In addition, this procedure enforces the generalized consistency conditions, $\dot{f}$ and $\dot{g}$, in the sense of distributions, i.e. f and g are satisfied at the end of the loading step. Furthermore, in this approach there is no need to consider $\dot{\phi}$ and T as additional degrees of freedom. Therefore, by using this approach, one does not need to introduce high-order continuous shape functions (e.g. C^1 class or penalty-enhanced C^0 class functions) for the calculation of higher-order gradients in the finite element context as is usually adopted for the gradient-dependent models based on the work of de Borst and co-workers (see e.g. [15,18,17,16]).

To evaluate the gradients $\nabla^2 \dot{\phi}$ and $\nabla^2 T$ at integration point m, the values of $\dot{\phi}$ and T at m as well as the values at the neighboring points (nonlocality) are needed. The Laplacian at m is evaluated from the derivatives of a polynomial function that interpolates the values of $\dot{\phi}$ and T at the neighboring points. Therefore, $\nabla^2 \dot{\phi}_{(m)}$ and $\nabla^2 T_{(m)}$, can be expressed in terms of $\dot{\phi}_{(n)}$ and $T_{(n)}$ with $n \in \{1, \ldots, N_{GP}\}$ using the following relations:

$$\nabla^2 \dot{\phi}_{(m)} = \sum_{n=1}^{N_{GP}} G_{(mn)} \dot{\phi}_{(n)}, \quad \nabla^2 T_{(m)} = \sum_{n=1}^{N_{GP}} G_{(mn)} T_{(n)} \tag{67}$$

where N_{GP} is the number of Gauss integration points and the coefficients matrix $G_{(mn)}$ depends on the current coordinates of the Gauss integration points. Abu Al-Rub and Voyiadjis [5] have derived $G_{(mn)}$ for two-dimensional problems assuming a complete second-order polynomial function as

$$G_{(mn)} = 2[\text{5th Row of } \boldsymbol{H}^{-1} + \text{6th Row of } \boldsymbol{H}^{-1}]\nu_{(n)} \tag{68}$$

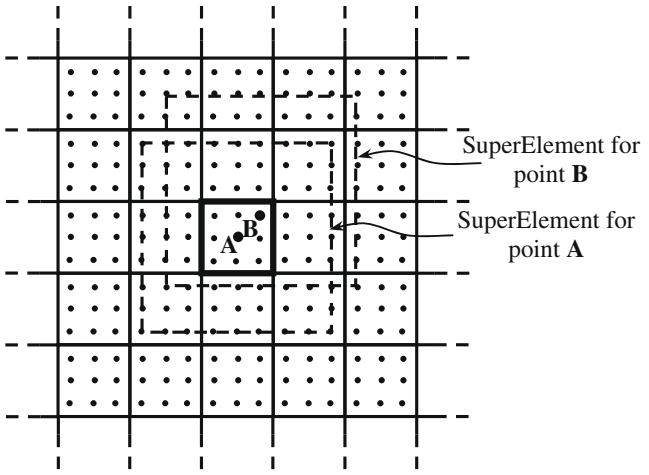

Fig. 3. A schematic illustration for the computation of the Laplacian terms from a regular finite element mesh.

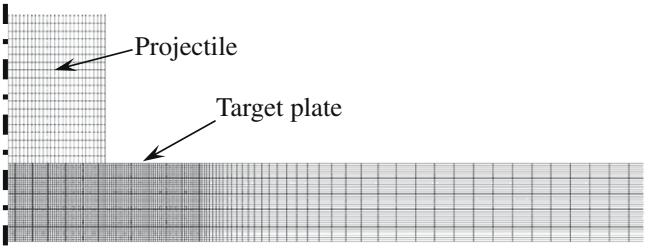

Fig. 4. Finite element mesh plot of the axisymmetric initial configuration just before impact.

where $\boldsymbol{v}$ is the variables vector $\boldsymbol{v}^T = \lfloor 1 \quad x \quad y \quad xy \quad x^2 \quad y^2 \rfloor$ with x and y coordinates, and $\boldsymbol{H}$ is a symmetrical square matrix given by

$$\boldsymbol{H} = \sum_{n=1}^{N_{GP}} \nu_{(n)} (\nu_{(n)})^T = \sum_{n=1}^{N_{GP}} \begin{bmatrix} 1 & x_n & y_n & x_n y_n & x_n^2 & y_n^2 \\ & x_n^2 & x_n y_n & x_n^2 y_n & x_n^3 & x_n y_n^2 \\ & & y_n^2 & x_n y_n^2 & x_n^2 y_n & y_n^3 \\ & & & x_n^2 y_n^2 & x_n^3 y_n & x_n y_n^3 \\ & \text{Symm} & & & x_n^4 & x_n^2 y_n^2 \\ & & & & & y_n^4 \end{bmatrix} \tag{69}$$

Fig. 3 shows a schematic illustration for the computation of the Laplacian terms from a regular finite element mesh, where $\nabla^2 \dot{\phi}$ and $\nabla^2 T$ are calculated at the integration points of each element based on the neighboring elements. For example, if four-nodded element with nine integration points (full integration) is assumed for a two-dimensional problem, a superelement of eight neighboring elements with total 81 integration points can be used to calculate the Laplacians at each integration point. Except for each corner and mid-boundary elements, the total number of integration points from the surrounding elements will be different. This illustration is valid for any element with any number of integration points. However, with more integration points, higher accuracy is achieved. This illustration is valid for one-dimensional as well as for three-dimensional mesh discretizations.

6.3. Computational algorithm

In this section, an algorithmic treatment of the heat equation, Eq. (61), and the consistency conditions in Eqs. (64) and (66) based on the calculation of $\nabla^2 \dot{\phi}$ and $\nabla^2 T$ from Eq. (67) is presented.

Therefore, Eqs. (61), (64) and (66) can be rewritten, respectively, at each integration point m as follows:

$$\boldsymbol{Q}^{(i)}_{1(m)} : \boldsymbol{d}_{(m)} + Q^{t(i)}_{1(m)} \sum_{n=1}^{N_{GP}} G^{(i)}_{(mn)} T_{(n)} - \frac{1}{\Delta t}(T - T_r) + Q^{p(i)}_{1(m)} \dot{p} + Q^{d(i)}_{1(m)} \dot{\phi} + Q^{d(i)}_{2(m)} \sum_{n=1}^{N_{GP}} G^{(i)}_{(mn)} \dot{\phi}_{(n)} = 0 \tag{70}$$

$$\boldsymbol{Q}^{(i)}_{2(m)} : \boldsymbol{d}_{(m)} + Q^{t(i)}_{2(m)} \sum_{n=1}^{N_{GP}} G^{(i)}_{(mn)} T_{(n)} + Q^{p(i)}_{2(m)} \dot{p} + Q^{d(i)}_{3(m)} \dot{\phi} + Q^{d(i)}_{4(m)} \sum_{n=1}^{N_{GP}} G^{(i)}_{(mn)} \dot{\phi}_{(n)} = 0 \tag{71}$$

$$\boldsymbol{Q}^{(i)}_{3(m)} : \boldsymbol{d}_{(m)} + Q^{t(i)}_{3(m)} \sum_{n=1}^{N_{GP}} G^{(i)}_{(mn)} T_{(n)} + Q^{p(i)}_{3(m)} \dot{p} + Q^{d(i)}_{5(m)} \dot{\phi} + Q^{d(i)}_{6(m)} \sum_{n=1}^{N_{GP}} G^{(i)}_{(mn)} \dot{\phi}_{(n)} = 0 \tag{72}$$

Note that (m) indicates the integration point, (i) indicates the previous iteration number, and $\boldsymbol{d}$, T, $\dot{p}$, and $\dot{\phi}$ at iteration $(i+1)$.

Also, for ease of numerical implementation, one can simply rewrite Eqs. (70)–(72), respectively, as follows:

$$\boldsymbol{N}^{tt(i)}\boldsymbol{\Lambda}^t + \boldsymbol{N}^{tp(i)}\boldsymbol{\Lambda}^p + \boldsymbol{N}^{td(i)}\boldsymbol{\Lambda}^d = \boldsymbol{Z}^{t(i)} \tag{73}$$

$$\boldsymbol{N}^{pt(i)}\boldsymbol{\Lambda}^t + \boldsymbol{N}^{pp(i)}\boldsymbol{\Lambda}^p + \boldsymbol{N}^{pd(i)}\boldsymbol{\Lambda}^d = \boldsymbol{Z}^{p(i)} \tag{74}$$

$$\boldsymbol{N}^{dt(i)}\boldsymbol{\Lambda}^t + \boldsymbol{N}^{dp(i)}\boldsymbol{\Lambda}^p + \boldsymbol{N}^{dd(i)}\boldsymbol{\Lambda}^d = \boldsymbol{Z}^{d(i)} \tag{75}$$

Combining Eqs. (73)–(75), one obtains

$$\begin{bmatrix} \boldsymbol{N}^{tt(i)} & \boldsymbol{N}^{tp(i)} & \boldsymbol{N}^{td(i)} \\ \boldsymbol{N}^{pt(i)} & \boldsymbol{N}^{pp(i)} & \boldsymbol{N}^{pd(i)} \\ \boldsymbol{N}^{dt(i)} & \boldsymbol{N}^{dp(i)} & \boldsymbol{N}^{dd(i)} \end{bmatrix} \begin{Bmatrix} \boldsymbol{\Lambda}^t \\ \boldsymbol{\Lambda}^p \\ \boldsymbol{\Lambda}^d \end{Bmatrix} = \begin{Bmatrix} \boldsymbol{Z}^{t(i)} \\ \boldsymbol{Z}^{p(i)} \\ \boldsymbol{Z}^{d(i)} \end{Bmatrix} \tag{76}$$

where

$$\boldsymbol{\Lambda}^t = \lfloor\, T_{(1)} \quad T_{(2)} \quad \cdots \quad T_{(N_{GP})} \,\rfloor^T \tag{77}$$

$$\boldsymbol{\Lambda}^p = \lfloor\, \dot{p}_{(1)} \quad \dot{p}_{(2)} \quad \cdots \quad \dot{p}_{(N_{GP})} \,\rfloor^T \tag{78}$$

$$\boldsymbol{\Lambda}^d = \lfloor\, \dot{\phi}_{(1)} \quad \dot{\phi}_{(2)} \quad \cdots \quad \dot{\phi}_{(N_{GP})} \,\rfloor^T \tag{79}$$

$$\boldsymbol{Z}^{t(i)} = \left\lfloor\, Z^{t(i)}_{(1)} \quad Z^{t(i)}_{(2)} \quad \cdots \quad Z^{t(i)}_{(N_{GP})} \,\right\rfloor^T \tag{80}$$

$$\boldsymbol{Z}^{p(i)} = \left\lfloor\, Z^{p(i)}_{(1)} \quad Z^{p(i)}_{(2)} \quad \cdots \quad Z^{p(i)}_{(N_{GP})} \,\right\rfloor^T \tag{81}$$

$$\boldsymbol{Z}^{d(i)} = \left\lfloor\, Z^{d(i)}_{(1)} \quad Z^{d(i)}_{(2)} \quad \cdots \quad Z^{d(i)}_{(N_{GP})} \,\right\rfloor^T \tag{82}$$

with the components of Eqs. (80)–(82) are presented in Eq. (B.1) and the components of the big matrix in the left-hand of Eq. (76) are presented in Eqs. (B.2)–(B10). Although the calculation of the components of Eq. (76) is lengthy, but it is straightforward. Moreover, the linear system of equations in Eq. (76) can be solved simply for $\boldsymbol{\Lambda}^t, \boldsymbol{\Lambda}^p$, and $\boldsymbol{\Lambda}^d$ using a numerical iterative scheme such as the Gauss–Jordan iterative method. The final solution are obtained when the following conditions are met

$$\sum_{n=1}^{N_{GP}} \left\| T^{(i+1)}_{(n)} - T^{(i)}_{(n)} \right\| \leqslant TOL, \quad \sum_{n=1}^{N_{GP}} f_{(n)} \leqslant TOL, \quad \sum_{n=1}^{N_{GP}} g_{(n)} \leqslant TOL \tag{83}$$

where $\|\ \|$ is the error norm, f and g are the viscoplastic and viscodamage conditions in Eqs. (44) and (47), respectively, and TOL could be set to a very small value in the order of 10^{-5}. This concludes the computational algorithm for calculating T, $\nabla^2 T$, $\dot{p}$, $\dot{\phi}$, and $\nabla^2\dot{\phi}$, which are necessary for updating the final stress and updating the values of the constitutive variables.

The formulated numerical algorithms presented here are coded as a VUMAT user material subroutine in the commercial finite element code Abaqus/Explicit [1]. Abaqus/Explicit is mainly used for high transient dynamic problems and it uses explicit integration algorithms. For information about writing the VUMAT subroutine consult the reference manuals of Abaqus [1].

It is noteworthy that a local damage model is obtained by simply setting a zero value for the length scale parameter in the proposed model (i.e. setting $\ell = 0$). The ability of the local damage model versus the nonlocal damage model in simulating plugging failure in ballistic penetration is demonstrated next.

7. Numerical simulation of plugging failure in ballistic penetration

The objective of this numerical example is to show that the proposed constitutive equations are able to predict the ballistic limit of a blunt projectile impacting a target independent of the finite element mesh density used in the finite element simulations and to compare the predictions from the local damage model (i.e. when setting the length scale $\ell = 0$) with the nonlocal damage model. This is done by conducting numerical simulation of the experimental tests performed by Børvik et al. [10] on the effect of target thickness in blunt projectile made of hardened Arne tool steel penetration Weldox 460 E high-strength steel circular plates.

The model material constants of the target material and the projectile material are listed in Table 1. For simplicity, the projectile is modeled as a bilinear elastic–plastic strain rate-independent von Mises material (i.e. linear hardening modulus h and fracture strain ε_f), which is already implemented in Abaqus/Explicit code. The values for $\overline{K} = \overline{E}/3(1-2\bar{\nu})$ and $\overline{G} = \overline{E}/2(1+\bar{\nu})$ with $\overline{E}$ is the Young's modlus and $\bar{\nu}$ is the Poisson's ratio for the effective undamaged material, T_r, T_m, α_t, k, ρ_o, c_v, c_p, $\gamma = c_p/c_v$, $\eta^{vp} = \eta^{vd}$, $m_1 = m_2$, $n_1 = n_2$, σ_{yp}, and ϕ_c are as reported by Børvik et al. [9] based on standard tensile tests on smooth and notched specimens at different strain rates and temperatures. It is found that the static strain rate at which the target material becomes rate-independent is 10^{-5} s^{-1} at $T_r = 295$ K. In order to maintain

Table 1
Material constants for target and projectile materials.

Target material of Weldox 460 E steel			
$\overline{E} = 200$ GPa	$\alpha_t = 1.1 \times 10^{-5}$/K	$\phi^c = 0.30$	$B = 0.4$
$\bar{\nu} = 0.33$	$c_p = 452$ J/kg K	$k_B = 1.38 \times 10^{-23}$ J/K	$k = 36$ W/m K
$\sigma_{yp} = 490$ MPa	$c_v = 266$ J/kg.K	$P_{\text{cutoff}} = 160$ GPa	$p = 0.5$
$T_r = 295$ K	$\gamma = 1.7$	$\beta = 2$	$q = 1.5$
$T_m = 1800$ K	$m_1 = m_2 = 0.941$	$Q = 14$ MPa	$n = 0.72$
$\rho_o = 7850$ kg/m^3	$n_1 = n_2 = 1$	$a = 8$	
$\eta^{vp} = \eta^{vd} = 0.01$ s	$\eta_r = 0$	$Y^{th} = 1.2$ J/m^3	
Projectile material of hardened arne tool steel			
$\overline{E} = 204$ GPa	$\bar{\nu} = 0.33$	$\rho_o = 7850$kg/m^3	$\sigma_{yp} = 1900$ MPa
$h = 15$ GPa	$\varepsilon_f = 2.15\%$		

Table 2
Summary of ballistic limit mesh sensitivity results.

Thickness of plates (mm)	Smallest element size (mm^2)	Number of element through the thickness	Ballistic limit velocity (mm/s)		
			Experimental	Local damage[a]	Nonlocal damage[a]
8	0.25 × 0.25	32	154.3	185 (19.9)	162 (5)
	0.20 × 0.20	40	154.3	177.5 (15)	160 (3.7)
	0.16 × 0.16	50	154.3	167.5 (8.6)	157 (1.7)
	0.10 × 0.10	80	154.3	155 (0.5)	155 (0.5)
12	0.25 × 0.25	48	184.5	187.5 (1.6)	187 (1.4)
	0.20 × 0.20	60	184.5	187.5 (1.6)	187.5 (1.6)
	0.16 × 0.16	75	184.5	169 (8.4)	185 (0.3)
16	0.40 × 0.40	40	239.6	242.5 (1.2)	241 (0.6)
	0.32 × 0.32	50	239.6	227.5 (5.1)	235 (1.9)
	0.25 × 0.25	64	239.6	217.5 (9.2)	245 (2.3)

[a] Value between brackets indicates percentage error as compared to the experimental data. Experimental data are by Børvik et al. [10].

the nonlocality of the damage driving force in Eq. (39) or (40), a value of 2 is assumed for the damage exponent β. The values for the parameters Q and a associated with the plasticity isotropic hardening function R in Eq. (37) are obtained from Voyiadjis et al. [41]. In the damage nucleation condition, Eq. (47), Y^{th} is calculated from $Y^{th} = \beta\sigma_{yp}^2/2\bar{E}$ at yielding whereas the damage growth rate parameter B is calibrated based on close agreement between the predicted and the experimental ballistic limit velocities. Also, the mean grain size and precipitate inter-particle size in Eq. (53) are taken from Børvik et al. [8] to be d = 10 μm and D = 1 μm such that an initial value for ℓ = 10 μm is obtained.

In these simulations a four-node 2D axisymmetric element with one integration point and a stiffness based on hourglass control is used. Plot of the initial configuration, showing a part of the target plate and the blunt projectile just prior to impact, is shown in Fig. 3. Three target plates of nominal thicknesses of 8, 12, and 16 mm and a diameter of 500 mm are simulated, while the nominal length and diameter of the hardened projectile are 80 mm and 20 mm, respectively. In each run, the target plate is fully clamped at the edge boundaries, while the projectile is given an initial velocity similar to the one used in the corresponding experiment conducted by Børvik et al. [10]. Different finite element mesh-densities are used in studying the mesh sensitivity of the ballistic limit velocity predictions. In fact, the simulations conducted by Børvik et al. [10] with the Johnson and Cook model [19] have shown a strong mesh-dependency of the ballistic limit velocities due to strain localization and plugging for blunt projectiles. To check this, the smallest element size directly beneath the projectile and the number of elements of constant size through the target thickness are outlined in Table 2 for each plate thickness. In order to reduce the computational time, which is affected both by the element size and number, the mesh was somewhat coarsened towards the boundary. Contact was modeled using an automatic 2D single surface penalty formulation available in Abaqus/Explicit [1]. A friction coefficient of 0.05 is assumed between the projectile and the target. Time increments of order 10^{-8} s are used to satisfy the stability criteria. Furthermore, to allow crack growth during penetration, an element erosion algorithm based on the proposed failure criteria is used to remove the failed elements from the mesh.

Figs. 5–7 show the impact versus the predicted residual velocity curves for targets with thicknesses 8, 12, and 16 mm, respectively, for the various number of elements through the plate thickness when compared to the experimental data by Børvik et al. [10]. Figs. 5(a), 6(a) and 7(a) show the current model predictions when assuming a zero length scale ℓ = 0 (i.e. local damage), while Figs. 5(b), 6(b) and 7(b) show the predictions with the nonlocal damage model. It is very clear that mesh sensitivity is most distinct close to the ballistic limit such that the predicted ballistic limit velocity (i.e. at zero residual velocity) when assuming ℓ = 0 is mesh sensitive. At higher impact velocities, the results are far less affected by the mesh size. However, this mesh sensitivity is alleviated to a great extent when using $\ell \neq 0$ (i.e. nonlocal damage). The predicted ballistic limit velocities for the three plate thicknesses when using local versus nonlocal damage are listed in Table 2 and compared with experimental values. Also, it is seen from Figs. 5(a), 6(a) and 7(a) that the mesh-sensitivity increases as the target thickness in-

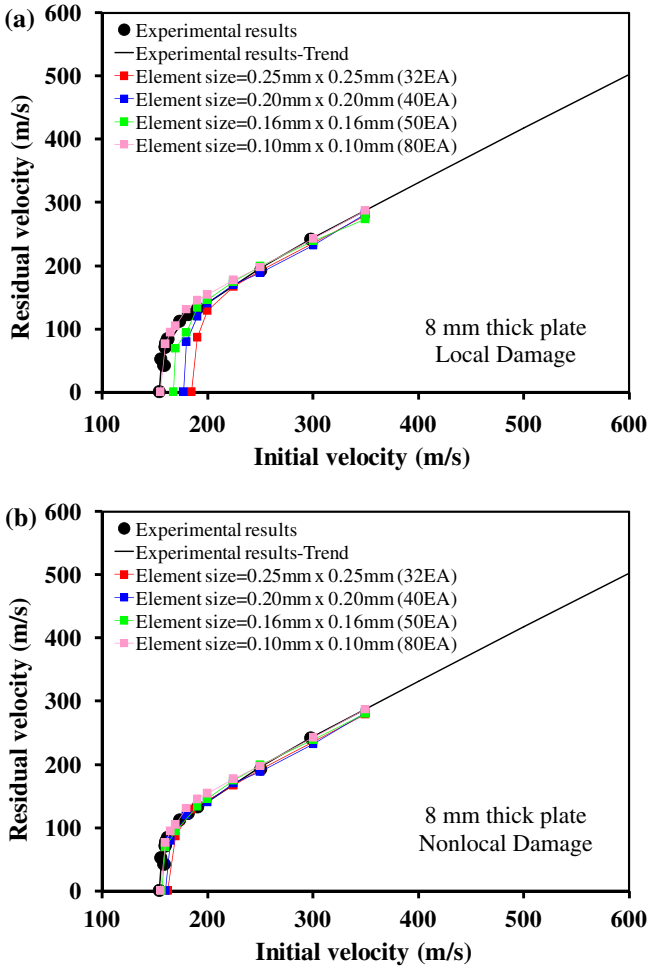

Fig. 5. Mesh sensitivity study of the blunt residual velocity versus its initial impact velocity impacting a 8 mm thick target when using (a) local damage and (b) nonlocal damage. Experimental data are after Børvik et al. [10].

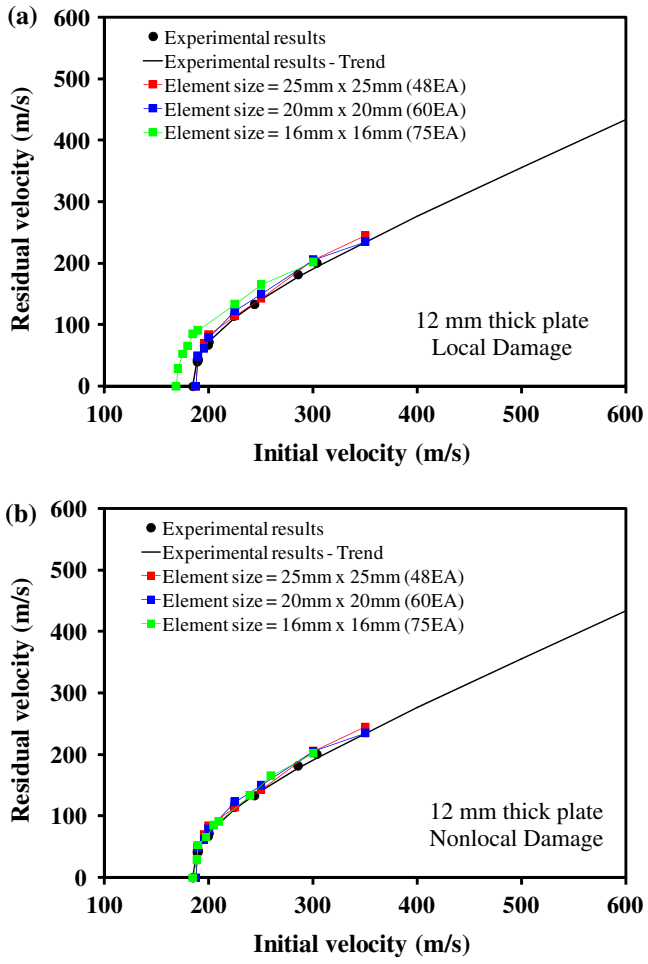

Fig. 6. Mesh sensitivity study of the blunt residual velocity versus its initial impact velocity impacting a 12 mm thick target when using (a) local damage and (b) nonlocal damage. Experimental data are after Børvik et al. [10].

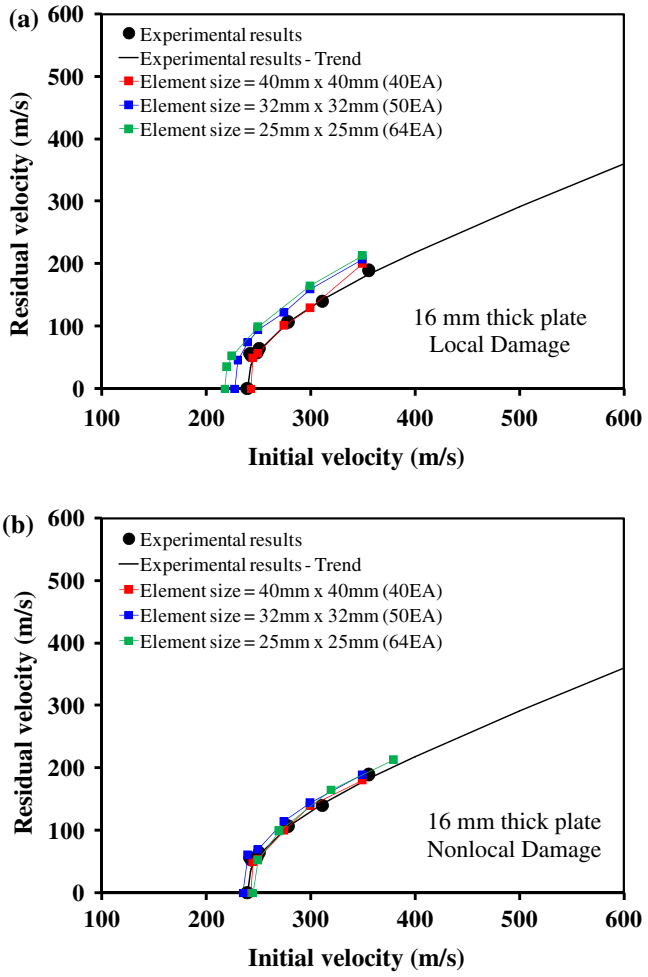

Fig. 7. Mesh sensitivity study of the blunt residual velocity versus its initial impact velocity impacting a 16 mm thick target when using (a) local damage and (b) nonlocal damage. Experimental data are after Børvik et al. [10].

creases and the ballistic limit velocity decreases as the number of elements through the thickness increases. Therefore, when conducting the ballistic failure simulations using a local damage model, one does not know which mesh density will yield meaningful values for the ballistic limit velocity, which may mislead the design of ballistic protective systems. The proposed nonlocal damage model successfully predicts meaningful values for the ballistic limit; of course, when mesh of sufficient density is used. Also, the nonlocal theory can be used in reducing the computational time by using coarser meshes.

The observed mesh sensitivity is due to plastic strain localization and plugging for blunt projectile where the length scale parameter ℓ plays the role of a localization limiter. Although, the current viscoplasticity theory, viscodamage theory, and heat conduction implicitly introduce length scale parameters or localization limiters (e.g. [23,24,33,41]), they are not sufficient in eliminating the mesh-dependency problem. Moreover, those theories cannot be used alone to predict size-scale effects in heterogeneous materials (e.g. particle size effect in materials with dispersed hard particles at decreasing microstructural length scales or metal matrix composites). Also, it can be seen from Figs. 5(a), 6(a) and 7(a) that the mesh sensitivity starts to disappear at higher impact speeds than the ballistic limit. In fact, mesh-objective results are obtained after a transition point (jump in residual velocity at the ballistic limit) in the impact velocity-residual velocity curve at which the mode of failure is changing from shear plugging to more of an expansion of a cavity mode with limited plastic shear localization. Therefore, one expects that the ballistic limit mesh-dependency is less for hemispherical and conical projectile shapes. This will be investigated in a future work.

Fig. 8 shows the perforation processes of the 8 mm thick plate with minimum element size of 0.1×0.1 mm^2 impacted by a blunt projectile with a velocity of 174 m/s, which is slightly higher than the experimental ballistic limit. As shown, the simulations qualitatively agree with the high-speed camera images from Børvik et al. [10].

Numerical plots showing perforation of the target plates with different thickness are given in Figs. 9–11 for thicknesses 8, 12, and 16 mm, respectively. The contours of normalized nonlocal damage density, $\widetilde{\phi}/\phi_c$, are plotted on the deformed geometry. It can be seen that limited damage occurs outside the localized shear zone. Also, it is seen that the extension of the localized damage zone increases and the global target deformation decreases with increasing target thickness. These plots compare well with the high-speed camera images in Børvik et al. [10]. These plots clearly demonstrate that the proposed model qualitatively captures the overall physical behavior of the target during penetration, perforation, shear localization, crack propagation, and complete failure. Notice also that in these plots, only a part of the complete target plate is shown. Similar qualitative results, not shown here, are obtained by using the local damage model.

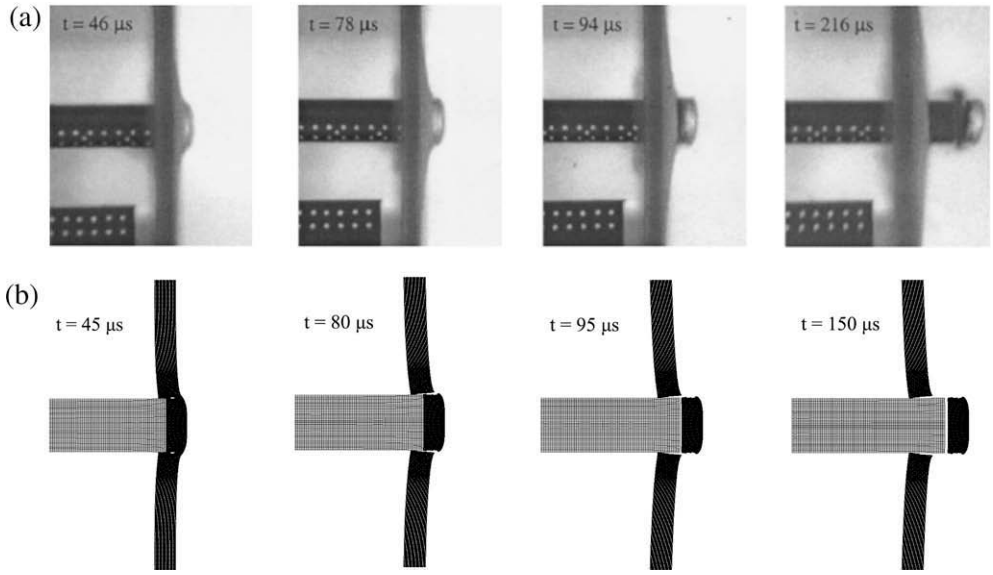

Fig. 8. Perforation process of 8 mm thick plate impacted by a blunt projectile with a velocity of 174 m/s just above the ballistic limit. (a) Experimental (Børvik et al. [10]) and (b) simulations.

8. Conclusions

A coupled thermo-hypoelasto-viscoplastic and nonlocal gradient-dependent thermo-viscodamage continuum model is developed in this paper for simulating the ballistic behavior of heterogeneous materials with length scale effects. It is concluded in this paper that an explicit material length scale parameter should be incorporated into the local theories of viscoplasticity and viscodamage in order to predict meaningful values for the ballistic limit velocities independent of the finite element mesh density. Although the proposed constitutive equations incorporate length scale parameters implicitly through the viscosity and heat conduction, they are insufficient in predicting mesh objective results of the ballistic behavior of high-strength steel targets impacted by blunt projectiles in which shear plugging due to plastic and damage localization is the dominant mode of failure. This mesh sensitivity is more significant at impact velocities close to the ballistic limit velocity and increases as the target thickness increases. This is attributed to the larger plastic and damage localization as the target thickness increases. Hence, in case of absence of experimental data to check the ballistic results from a specific mesh density, one cannot know if the local model underestimates (conservative) or overestimates (unconservative) the value of the ballistic limit velocity. However, an explicit length scale parameter through the nonlocal damage theory sufficiently alleviates the mesh sensitivity of the ballistic limit velocity allowing one to precisely determine the ballistic limit velocities and describe the overall physical ballistic behavior of targets using numerical simulations. Moreover, it can be concluded that the ballistic limit prediction from the nonlocal theory is a slightly conservative one since it takes into consideration the current damage at a specific point as well as the effect of the surrounding damaged region at that point. Therefore, this desirable feature provided by the nonlocal theory does lead to an improvement in the modeling and numerical simulation of high velocity impact related problems such that numerical simulations could be used in the design process of protective systems against high speed impacts and in providing physical understanding of the ballistic and penetration problem.

In general, it can be seen that close agreement between the numerical and experimental results is achieved. Hence, the consti-

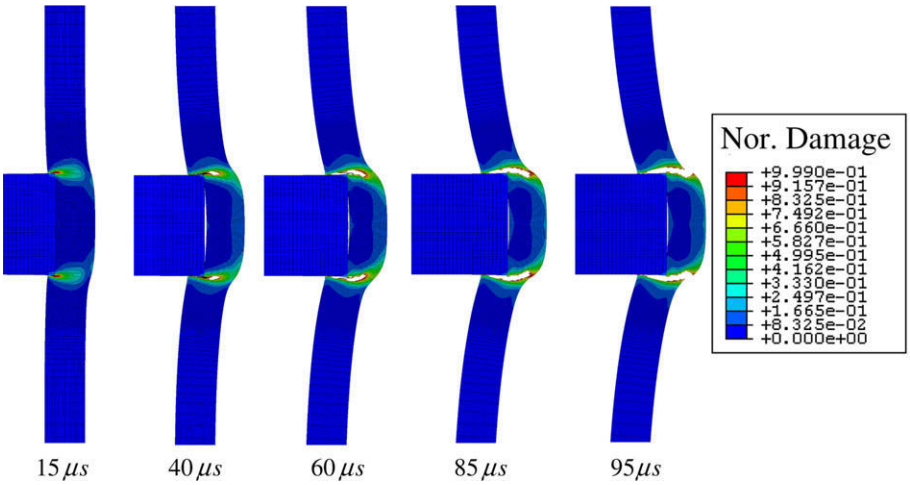

Fig. 9. Perforation of the 8 mm target plate by a blunt projectile of initial impact velocity of 190 m/s plotted as contours of the normalized nonlocal damage density.

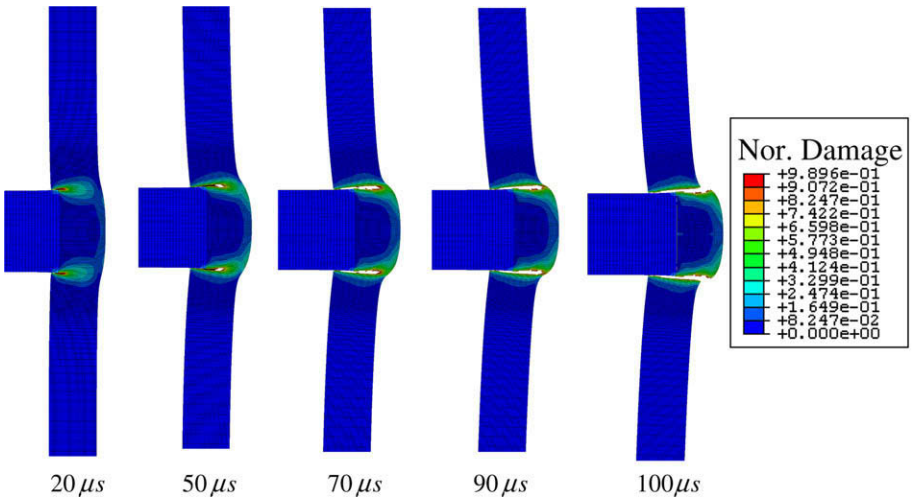

Fig. 10. Perforation of the 12 mm target plate by a blunt projectile of initial impact velocity of 190 m/s plotted as contours of the normalized nonlocal damage density.

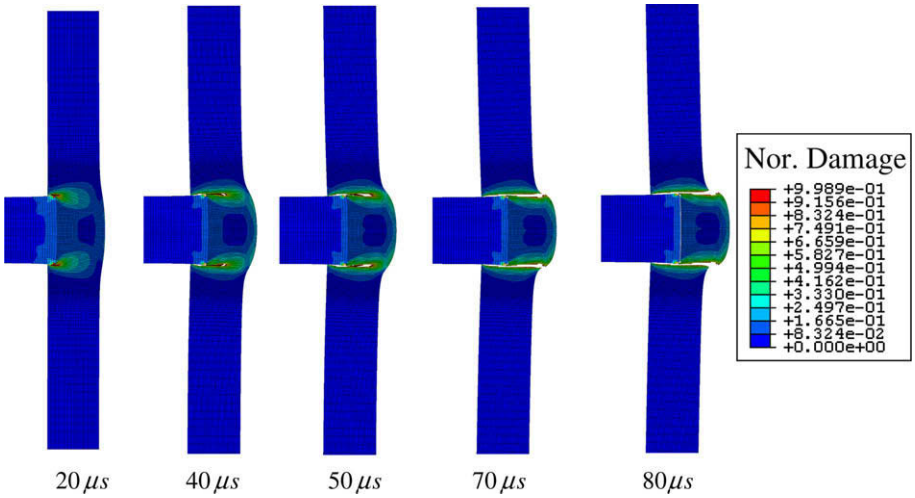

Fig. 11. Perforation of the 16 mm target plate by a blunt projectile of initial impact velocity of 250 m/s plotted as contours of the normalized nonlocal damage density.

tutive model and computational methodology presented in this paper work well for ductile targets perforated by deformable or rigid blunt projectiles. However, different set of experiments need to be simulated in order to draw solid conclusions. More elaborate study using the current constitutive and computational model is needed for simulating high-speed impacts using different projectile nose shapes (e.g. hemispherical and conical) and targets with different materials. Also, the proposed model can be used to study long or short penetrators, thin or thick targets, normal or oblique impacts, ductile or brittle materials, different velocity regions, different types of projectiles, etc.

Acknowledgments

The work reported in this paper is supported by a joint grant from the US National Science Foundation and the US Department of Energy (NSF #0728032). Also, this research is supported by a grant from the US Army Research Office. These supports are gratefully acknowledged.

Appendix A

From the heat balance equation we have

$$\mathbf{Q}_1 = \frac{1}{\rho_o c_p}[T\partial_T\boldsymbol{\tau} + (P - T\partial_T P)J^e\mathbf{1}] \tag{A.1}$$

$$Q_1^p = \frac{1}{\rho_o c_p}\left[\{(\boldsymbol{\tau} - T\partial_T\boldsymbol{\tau}) - (P - T\partial_T P)J^e\mathbf{1}\} : T\partial_{\boldsymbol{\tau}} f - (R - T\partial_T R)\right] \tag{A.2}$$

$$Q_1^d = \frac{1}{\rho_o c_p}\left[\{(\boldsymbol{\tau} - T\partial_T\boldsymbol{\tau}) - (P - T\partial_T P)J^e\mathbf{1}\} : T\partial_{\boldsymbol{\tau}} g + \left(\widehat{Y} - T\partial_T \widehat{Y}\right)\right] \tag{A.3}$$

From the viscoplasticity generalized consistency condition we obtain

$$\mathbf{Q}_2 = \partial_{\boldsymbol{\tau}} f : \overline{\boldsymbol{E}} + (\partial_T f)\mathbf{Q}_1 \tag{A.4}$$

$$Q_2^p = Q_1^p\partial_T f - \partial_{\boldsymbol{\tau}} f : \overline{\boldsymbol{E}} : \partial_{\boldsymbol{\tau}} f - b(Q - R) + \partial_{\dot{p}} f/\Delta t \tag{A.5}$$

$$Q_3^d = Q_1^d\partial_T f - \partial_{\boldsymbol{\tau}} f : \overline{\boldsymbol{E}} : \partial_{\boldsymbol{\tau}} g \tag{A.6}$$

From the viscodamage generalized consistency condition we have

$$\boldsymbol{Q}_3 = \partial_{\bar{\tau}} g : \overline{\boldsymbol{E}} + \left(\partial_T g - 3\overline{K}\alpha_t \partial_{\bar{\tau}} g : \mathbf{1}\right)\boldsymbol{Q}_1 \tag{A.7}$$

$$Q_3^p = Q_1^p\left(\partial_T g - 3\overline{K}\alpha_t \partial_{\bar{\tau}} g : \mathbf{1}\right) - \partial_{\bar{\tau}} g : \overline{\boldsymbol{E}} : \partial_{\bar{\tau}} f + \partial_{\hat{p}} g/\Delta t \tag{A.8}$$

$$Q_4^d = Q_1^d\left(\partial_T g - 3\overline{K}\alpha_t \partial_{\bar{\tau}} g : \mathbf{1}\right) - \partial_{\bar{\tau}} g : \overline{E} : \partial_{\bar{\tau}} g + \partial_{\hat{\phi}} g \tag{A.9}$$

Appendix B

The following equations details the components of Eq. (76):

$$\begin{aligned} Z_{(m)}^{t(i)} &= -\boldsymbol{Q}_{1(m)}^{(i)} : \boldsymbol{d}_{(m)} - \frac{1}{\Delta t} T_r, \\ Z_{(m)}^{p(i)} &= -\boldsymbol{Q}_{2(m)}^{(i)} : \boldsymbol{d}_{(m)}, \quad Z_{(m)}^{d(i)} = -\boldsymbol{Q}_{3(m)}^{(i)} : \boldsymbol{d}_{(m)} \end{aligned} \tag{B.1}$$

$$\boldsymbol{N}^{tt(i)} = \begin{bmatrix} Q_{1(1)}^{t(i)} G_{(11)} - 1/\Delta t & Q_{2(2)}^{t(i)} G_{(12)} & \cdots & Q_{1(N_{GP})}^{t(i)} G_{(1N_{GP})} \\ Q_{1(2)}^{t(i)} G_{(21)} & Q_{1(2)}^{t(i)} G_{(22)} - 1/\Delta t & \cdots & Q_{1(N_{GP})}^{t(i)} G_{(2N_{GP})} \\ \vdots & \vdots & \ddots & \vdots \\ Q_{1(N_{GP})}^{t(i)} G_{(N_{GP}1)} & Q_{1(N_{GP})}^{t(i)} G_{(2N_{GP})} & \cdots & Q_{1(N_{GP})}^{t(i)} G_{(N_{GP}N_{GP})} - 1/\Delta t \end{bmatrix} \tag{B.2}$$

$$\boldsymbol{N}^{tp(i)} = \begin{bmatrix} Q_{1(1)}^{p(i)} & 0 & \cdots & 0 \\ 0 & Q_{1(1)}^{p(i)} & \cdots & 0 \\ \vdots & \vdots & \ddots & \vdots \\ 0 & 0 & \cdots & Q_{1(N_{GP})}^{p(i)} \end{bmatrix} \tag{B.3}$$

$$\boldsymbol{N}^{td(i)} = \begin{bmatrix} Q_{1(1)}^{d(i)} + Q_{2(1)}^{d(i)} G_{(11)} & Q_{2(2)}^{d(i)} G_{(12)} & \cdots & Q_{2(N_{GP})}^{d(i)} G_{(1N_{GP})} \\ Q_{2(2)}^{d(i)} G_{(21)} & Q_{1(1)}^{d(i)} + Q_{2(2)}^{d(i)} G_{(22)} & \cdots & Q_{2(N_{GP})}^{d(i)} G_{(2N_{GP})} \\ \vdots & \vdots & \ddots & \vdots \\ Q_{2(N_{GP})}^{d(i)} G_{(N_{GP}1)} & Q_{2(N_{GP})}^{d(i)} G_{(2N_{GP})} & \cdots & Q_{1(N_{GP})}^{d(i)} + Q_{2(N_{GP})}^{d(i)} G_{(N_{GP}N_{GP})} \end{bmatrix} \tag{B.4}$$

$$\boldsymbol{N}^{pt(i)} = \begin{bmatrix} Q_{2(1)}^{t(i)} G_{(11)} & Q_{2(2)}^{t(i)} G_{(12)} & \cdots & Q_{2(N_{GP})}^{t(i)} G_{(1N_{GP})} \\ Q_{2(2)}^{t(i)} G_{(21)} & Q_{2(2)}^{t(i)} G_{(22)} & \cdots & Q_{2(N_{GP})}^{t(i)} G_{(2N_{GP})} \\ \vdots & \vdots & \ddots & \vdots \\ Q_{2(N_{GP})}^{t(i)} G_{(N_{GP}1)} & Q_{2(N_{GP})}^{t(i)} G_{(2N_{GP})} & \cdots & Q_{2(N_{GP})}^{t(i)} G_{(N_{GP}N_{GP})} \end{bmatrix} \tag{B.5}$$

$$\boldsymbol{N}^{pp(i)} = \begin{bmatrix} Q_{2(1)}^{p(i)} & 0 & \cdots & 0 \\ 0 & Q_{2(1)}^{p(i)} & \cdots & 0 \\ \vdots & \vdots & \ddots & \vdots \\ 0 & 0 & \cdots & Q_{2(N_{GP})}^{p(i)} \end{bmatrix} \tag{B.6}$$

$$\boldsymbol{N}^{pd(i)} = \begin{bmatrix} Q_{3(1)}^{d(i)} + Q_{4(1)}^{d(i)} G_{(11)} & Q_{4(2)}^{d(i)} G_{(12)} & \cdots & Q_{4(N_{GP})}^{d(i)} G_{(1N_{GP})} \\ Q_{4(2)}^{d(i)} G_{(21)} & Q_{3(1)}^{d(i)} + Q_{4(2)}^{d(i)} G_{(22)} & \cdots & Q_{4(N_{GP})}^{d(i)} G_{(2N_{GP})} \\ \vdots & \vdots & \ddots & \vdots \\ Q_{4(N_{GP})}^{d(i)} G_{(N_{GP}1)} & Q_{4(N_{GP})}^{d(i)} G_{(2N_{GP})} & \cdots & Q_{3(N_{GP})}^{d(i)} + Q_{4(N_{GP})}^{d(i)} G_{(N_{GP}N_{GP})} \end{bmatrix} \tag{B.7}$$

$$\boldsymbol{N}^{dt(i)} = \begin{bmatrix} Q_{3(1)}^{t(i)} G_{(11)} & Q_{3(2)}^{t(i)} G_{(12)} & \cdots & Q_{3(N_{GP})}^{t(i)} G_{(1N_{GP})} \\ Q_{3(2)}^{t(i)} G_{(21)} & Q_{3(2)}^{t(i)} G_{(22)} & \cdots & Q_{3(N_{GP})}^{t(i)} G_{(2N_{GP})} \\ \vdots & \vdots & \ddots & \vdots \\ Q_{3(N_{GP})}^{t(i)} G_{(N_{GP}1)} & Q_{3(N_{GP})}^{t(i)} G_{(2N_{GP})} & \cdots & Q_{3(N_{GP})}^{t(i)} G_{(N_{GP}N_{GP})} \end{bmatrix} \tag{B.8}$$

$$\boldsymbol{N}^{dp(i)} = \begin{bmatrix} Q_{3(1)}^{p(i)} & 0 & \cdots & 0 \\ 0 & Q_{3(1)}^{p(i)} & \cdots & 0 \\ \vdots & \vdots & \ddots & \vdots \\ 0 & 0 & \cdots & Q_{3(N_{GP})}^{p(i)} \end{bmatrix} \tag{B.9}$$

$$\boldsymbol{N}^{dd(i)} = \begin{bmatrix} Q_{5(1)}^{d(i)} + Q_{6(1)}^{d(i)} G_{(11)} & Q_{6(2)}^{d(i)} G_{(12)} & \cdots & Q_{6(N_{GP})}^{d(i)} G_{(1N_{GP})} \\ Q_{6(2)}^{d(i)} G_{(21)} & Q_{5(1)}^{d(i)} + Q_{6(2)}^{d(i)} G_{(22)} & \cdots & Q_{6(N_{GP})}^{d(i)} G_{(2N_{GP})} \\ \vdots & \vdots & \ddots & \vdots \\ Q_{6(N_{GP})}^{d(i)} G_{(N_{GP}1)} & Q_{6(N_{GP})}^{d(i)} G_{(2N_{GP})} & \cdots & Q_{5(N_{GP})}^{d(i)} + Q_{6(N_{GP})}^{d(i)} G_{(N_{GP}N_{GP})} \end{bmatrix}. \tag{B.10}$$

References

[1] Abaqus. User manual, version 6.7. Providence (RI): Habbitt, Karlsson and Sorensen, Inc.; 2007.

[2] Abu Al-Rub RK, Voyiadjis GZ. Analytical and experimental determination of the material intrinsic length scale of strain gradient plasticity theory from micro- and nano-indentation experiments. Int J Plasticity 2004;20(6):1139–82.

[3] Abu Al-Rub RK, Voyiadjis GZ. Determination of the material intrinsic length scale of gradient plasticity theory. Int J Multiscale Comput Eng 2004;2:377–400.

[4] Abu Al-Rub RK, Voyiadjis GZ. A finite strain plastic-damage model for high velocity impacts using combined viscosity and gradient localization limiters. Part I: theoretical formulation. Int J Damage Mech 2006;15:293–334.

[5] Abu Al-Rub RK, Voyiadjis GZ. A direct finite element implementation of the gradient plasticity theory. Int J Numer Meth Eng 2005;63(4):603–29.

[6] Abu Al-Rub RK, Kim S-M. Multi-scale constitutive and computational modeling of hypervelocity impact damage of steel targets. In: Collection of technical papers – AIAA/ASME/ASCE/AHS/ASC structures, structural dynamics and materials conference, AIAA-2008-1743; 2008.

[7] Abu Al-Rub RK. Modeling the particle size and interfacial hardening effects in metal matrix composites with dispersed particles at decreasing microstructural length scales. Int J Multiscale Comput Eng 2008; in press.

[8] Børvik T, Leinum JR, Solberg JK, Hopperstad OS, Langseth M. Observations on shear plug formation in Weldox 460 E steel plates impacted by blunt-nosed projectiles. Int J Impact Eng 2001;25:553–72.

[9] Børvik T, Langseth M, Hopperstad OS, Malo KA. Perforation of 12 mm thick steel plates by 20 mm diameter projectiles with flat, hemispherical and conical noses. Part I: experimental study. Int J Impact Eng 2002;27(1):19–35.

[10] Børvik T, Langseth M, Hopperstad OS, Malo KA. Effect of target thickness in blunt projectile penetration of Weldox 460 E steel plates. Int J Impact Eng 2003;28:413–64.

[11] Clayton JD. Dynamic plasticity and fracture in high density polycrystals: constitutive modeling and numerical simulation. J Mech Phys Solids 2005;53:261–301.

[12] Clayton JD. Modeling dynamic plasticity and spall fracture in high density polycrystalline alloys. Int J Solids Struct 2005;42:4613–40.

[13] Clayton JD. Two-scale modeling of effects of microstructure and thermomechanical properties on the dynamic performance of an aluminum alloy. Int J Mater Struct Integrity 2008; in press.

[14] Coleman B, Gurtin M. Thermodynamics with internal state variables. J Chem Phys 1967;47(2):597–613.

[15] de Borst R, Mühlhaus H-B. Gradient-dependent plasticity formulation and algorithmic aspects. Int J Numer Meth Eng 1992;35:521–39.

[16] de Borst R, Pamin J. Some novel developments in finite element procedures for gradient dependent plasticity. Int J Numer Meth Eng 1996;39:2477–505.

[17] de Borst R, Pamin J, Geers M. On coupled gradient-dependent plastcity and damage theories with a view to localization. Eur J Mech A 1999;18:939–62.

[18] de Borst R, Sluys LJ, Mühlhaus H-B, Pamin J. Fundamental issues in finite element analysis of localization of deformation. Eng Comput 1993;10:99–121.

[19] Johnson GR, Cook HW. Fracture characteristics of three metals subjected to various strains strain rates temperature and pressures. Eng Fract Mech 1985;21(1):31–48.

[20] Kachanov LM. On the creep fracture time. Izv Akad Nauk USSR Otd Tech 1958;8:26–31 [in Russian].

[21] Kachanov LM. Introduction to continuum damage mechanics. The Netherlands: Martinus Nijhoff Publishers; 1986.

[22] Lemaitre J, Chaboche J-L. Mechanics of solid materials. London: Cambridge University Press; 1990.

[23] LeMonds J, Needleman A. Finite element analysis of shear localization in rate and temperature dependent solids. Mech Mater 1986;5:339–61.

[24] LeMonds J, Needleman A. An analysis of shear band development incorporating heat conduction. Mech Mater 1986;5:363.

[25] Pamin J. Gradeitn-dependent plasticity in numerical simulation of localization phenomena, Dissertation, Delft University of Technology; 1994.

[26] Pamin J, Askes H, de Borst R. Two gradient plasticity theories discretized with the element-free Galerkin method. Comput Meth Appl Mech Eng 2003;192:2377–403.

[27] Pijaudier-Cabot TGP, Bazant ZP. Nonlocal damage theory. ASCE J Eng Mech 1987;113:1512–33.
[28] Peerlings RHJ, de Borst R, Brekelmans WAM, de Vree JHP. Gradient enhanced damage for quasi-brittle materials. Int J Numer Meth Eng [Wiley, London] 1996;39:3391–403.
[29] Perzyna P. The constitutive equations for rate-sensitive materials. Quart Appl Math 1963;20:321–32.
[30] Simo JC, Honein T. Variational formulation, discrete conservation laws, and path domain independent integrals for elasto-viscoplasticity. J Appl Mech 1990;57:488–97.
[31] Simo JC, Hughes TJR. Computational inelasticity. Interdisciplinary applied mathematics. New York: Springer; 1998.
[32] Sidoroff F. Description of anisotiopic damage application to elasticity. In: Hult J, Lemaitre J, editors. IUTAM colloqium on physical nonlinearities in structural analysis. Berlin: Springer; 1980. p. 237–44.
[33] Sluys LJ. Wave propagation, localization and dispersion in softening solids, Ph.D. thesis, Delft University of Technology, The Netherlands; 1992.
[34] Vogler TJ, Clayton JD. Heterogeneous deformation and spall of an extruded tungsten alloy: plate impact experiments and crystal plasticity modeling. J Mech Phys Solids 2008;56:297–335.
[35] Voyiadjis GZ, Abu Al-Rub RK. Nonlocal continuum damage and plasticity: theory and computation. Singapore: World Scientific; 2009.
[36] Voyiadjis GZ, Venson AR, Abu Al-Rub RK. Damage quantification in metal matrix composites. In: Gdoutos EE, editor. Recent advances in experimental mechanics. Dordrecht: Kluwer; 2002. p. 109–20.
[37] Voyiadjis GZ, Venson AR. Experimental damage investigation of a SiC–Ti aluminide metal matrix composite. Int J Damage Mech 1995;4:338–61.
[38] Voyiadjis GZ, Abed FH. Microstructral based models for bcc and fcc metals with temperature and strain rate dependency. Mech Mater 2005;37:355–78.
[39] Voyiadjis GZ, Abu Al-Rub RK, Palazotto AN. Non-local coupling of viscoplasticity and anisotropic viscodamage for impact problems using the gradient theory. Arch Mech 2003;55:39–89.
[40] Voyiadjis GZ, Abu Al-Rub RK, Palazotto AN. Thermodynamic formulations for non-local coupling of viscoplasticity and anisotropic viscodamage for dynamic localization problems using gradient theory. Int J Plasticity 2004;20:981–1038.
[41] Voyiadjis GZ, Abu Al-Rub RK, Palazotto AN. On the small and finite deformation thermo-elasto-viscoplasticity theory: algorithmic and computational aspects. Eur J Comput Mech 2006;15:945–87.
[42] Voyiadjis GZ, Kattan PI. Advances in damage mechanics: metals and metals matrix composites. Oxford: Elsvier; 1999.
[43] Voyiadjis GZ, Abu Al-Rub RK. A finite strain plastic-damage model for high velocity impacts using combined viscosity and gradient localization limiters. Part II: numerical aspects and simulations. Int J Damage Mech 2006;15:335–73.
[44] Voyiadjis GZ, Abu Al-Rub RK. Gradient plasticity theory with a variable length scale parameter. Int J Solids Struct 2005;42:3998–4029.
[45] Wang WM, Sluys LJ. Formulation of an implicit algorithm for finite deformation viscoplasticity. Int J Solids Struct 2000;37(48–50):7329–48.
[46] Zerilli FJ, Armstrong RW. Dislocation-mechanics-based constitutive relations for material dynamics calculations. J Appl Phys 1987;61(5):445–59.